CENTRO DE INVESTIGACION EN MATERIALES AVANZADOS
DEPARTAMENTO DE POSGRADO

Nanomaterials for Organic and Hybrid Solar Cells

By

Diego Barrera-Méndez

A dissertation submitted in fulfillment of the requirements of the degree of DOCTOR OF PHILOSOPHY IN NANOTECHNOLOGY.

Doctoral Committee:

Professor Margarita Sánchez-Domínguez, Chair

Professor Julia W. P. Hsu, Co-chair

Professor Eduardo Martínez-Guerra

Professor Fransisco Aguirre-Tostado

Professor Pavel Vorobiev

Professor Alfonso Pérez-García

Professor Lorena Garza-Tovar

Monterrey, N. L., Mexico. July, 2015

ABSTRACT

This Ph.D. research has focused on the development of new materials for alternative renewable energy using organic photovoltaics (OPVs). The first step was to established reliable fabrication and characterization methods of organic photovoltaic devices. The reproducibility of organic photovoltaic cell performance is one of the essential issues that must be achieved before engaging serious investigations of the applications of creative and challenging ideas.

Secondly, we thoroughly studied the surface chemistry of the underlying layer and its critical role on the morphology of the BHJ active layer. We showed that when the active layer (which consists of blends of poly(3-hexylthiophene) (P3HT) and phenyl-C60-butyric acid methyl ester (PCBM)) is deposited and annealed over a sol-gel ZnO electron transport layer surface made from monoethanolamine (MEA) containing precursor, PCBM clusters form during annealing and this phase segregation leads to a drastic reduction of OPV parameters due to both low charge generation and high bimolecular recombination. Rinsing the pyrolyzed ZnO films with solvents or using a ZnO recipe without MEA significantly reduced the formation of PCBM clusters and produced devices with good performance.

Third, we developed new materials suitable for low-temperature processing and large area deposition methods to be used as transport layer on OPVs. We achieved the synthesis of material suspensions suitable for large area deposition, with controlled size, stoichiometry,

and electronic properties using controlled oxidative dissolution of micron sized metal powders with H_2O_2 in n-butanol. The small nanoparticle diameters of 1-2 nm enabled solution processing of *n*-type WO_3 and MoO_3, and *p*-type NiO_x and CoO_x nanoparticle films on ITO with electronic properties comparable to solution processed and vacuum deposited counterparts, without the need for any post processing.

We also explored the synthesis of solution processed transition metal dichalcogenides for electronic application. We demonstrated the ability to synthesize MoS_2 nanoflakes by solvothermal method by microwave heating. The characterization techniques confirmed the presence of 2H phase and hexagonal crystalline structure. In addition, the MoS_2 nanoflake thickness was consistent with a single-layer flake.

By the end of this work, we achieved the improvement of key OPV parameters by reducing the phase segregation of the active layer. We carried out the synthesis of material suspensions suitable for large area deposition, with controlled size, stoichiometry, and electronic properties enabling a route towards low-cost OPV fabrication. We tested the use of films casted from these suspensions as transport layer for OPV obtaining similar performances as the commonly used vacuum deposited materials. Finally we accomplished the synthesis and characterization of layered graphene-like materials, with electronic, optical, mechanical and thermal properties that makes them suitable for flexible electronic applications. With all these results we have contributed to enable a route towards low-cost OPV and other electronics fabrication.

Table of Contents

List of Figures

Acknowledgements

I would like to thank Consejo Nacional de Ciencia y Tecnología and Instituto de Inovación y Transferencia de Tecnología for the funding support.

I would like to specially thank my advisors Prof. Julia Hsu and Prof. Margarita Sánchez for her patience and guidance during these years or work. They have always showed their trust and belief in me, that strongly motivated me to pursuit my goals.

I would like to thank Dr. Yun-Ju Lee for guiding me, teaching me, and spending so much time with me doing experiments, and discussing the results.

I would also like to thank our group members, Jian Wang, Liang Xu, Sampreetha Thampy, Kaiyuan Luo, Juan Yi, and Subhiksha Venkatasamy.

Special thanks to my family in Mexico, without their love and encouragement non of these would be possible.

Finally, I would like to thank my wife Silvia Olivas. Thank you for being my quests companion and life-partner.

1 Introduction

1.1 Overview and Motivation

Over the past decade, the field of renewable energy production experienced a rapid growth as a result of the increased awareness regarding the limited availability of fossil fuels, the negative impact on the environment induced by their use, and the high price volatility of oil[1]. Amongst renewable energy sources, photovoltaics (PV) represent one of the most promising technologies because it is an abundant and easily accessible source of power[2]. In addition of being plentiful, solar radiation is also widely available geographically, giving photovoltaic technology a significant portability and scalability advantage over other alternative energy technologies[3].

The major PV technology commercially available nowadays is crystalline silicon. It is mainly based on costly batch-to-batch semiconductor processing production techniques, and represents around 90% of the market[1,4]. Thus, finding an alternative PV technology is essential and organic photovoltaics (OPV) have acquired much attention in this area during the past decade[5]. OPV technologies combine manufacturing adaptability, the potential to be flexible, lightweight and semitransparent[2,3]. In addition to these qualities, the main property that makes this technology attractive is the potential to be manufactured in a continuous printing process by large area coating on low cost substrates, thus considerably less effort and production energy is needed for the fabrication process[6]. For comparison, a typical Si wafer production plant with a 30 cm wafer process has an annually processed area output of 88,000 m^2/year. A typical printing machine can produce the same area in 1-10h[3].

Oxide films used for the fabrication of OPVs are commonly deposited by thermal evaporation methods or sol-gel processes that require temperatures higher than 300 °C. These deposition methods inhibit one of the key assets of OPV technologies, which is the large-area potential manufacturing. A widely used substitute for vacuum processed oxide films is the poly(3,4-ethylenedioxythiophene):poly(styrenesulfonate) (PEDOT:PSS); unfortunately, PEDOT:PSS has been evidenced to initiate a number of degradation mechanisms in organic electronic devices which limit the device lifetime and cause severely reliability issues[7]. Consequently, there has been strong efforts to achieve low-temperature solution processed oxide films. Only a few have been reported such as ZnO nanoparticles[8-11], WO_3[12], MoO_3[13], and V_2O_5[14]; nevertheless, the performance of these solution processed films depends strongly on the type and quantity of organic additives during synthesis and post-processing steps.

Currently, the power conversion efficiency (PCE) and operational stability of OPV are considerably lower than those offered by silicon technology. Research scientists have been focused on improving the PCE and operational stability of the devices, with a recent report of 10.6% for tandem cell[15]. Although this value falls short of 25-30%

PCE level offered by inorganic PV cells, it may be sufficient for a feasible commercial proposition when substantially less expensive production budget for OPV is considered[2]. Besides PCE, a key issue faced by OPVs is the stability of the organic materials. Nevertheless, it is encouraging that some similar molecules containing chromophores are commonly used for automotive paints, and that organic light-emitting displays are demonstrating acceptable lifetimes under high injection currents[4].

In the following chapters, details about basic mechanisms of OPV and different approaches proposed to improve the PCE of these devices will be discussed. In addition, details about previous work performed in the last three years will be provided, and future research plan will be described.

1.2 OPV Basics

The basic structure of an OPV cell is shown in **Fig. 1.1**. Sunlight enters through the transparent electrode. The absorption then takes place in the active layer, the excitation caused by the absorbed photons results in the creation of excitons, which consists of a Coulombically attracted electron-hole pair. Excitons diffuse through the active layer with a diffusion length of about 5-10 nm in an organic material. The energy required to split an exciton is in the range of 100-400 meV compared to a few meV for crystalline inorganic semiconductors[16]. Room temperature thermal energy kT and typical applied electric field are not sufficient to dissociate these excitons[17]. In order to split excitons into free charge carriers, the energy can be provided in the presence of an electron accepting material with a different electron affinity than the donor material[16,17]. Because the typical exciton diffusion length in conjugated polymers is limited to ~10 nm, the donor and acceptor materials should form nanoscale interpenetrating networks within the whole photoactive layer to ensure an efficient dissociation of excitons[18]. In this sense bulk heterojunction (BHJ) has a conceptual advantage, the donor and acceptor materials are deposited such that their interface area is maximized while typical dimensions of phase separations are continuous and within the exciton diffusion range[19]. When excitons reach the interface between the donor and the acceptor, the electric field dissociates the exciton to form free charges (electron and hole). The free charges then transport to the cathode (electron) and anode (hole), so that a photocurrent is generated[20].

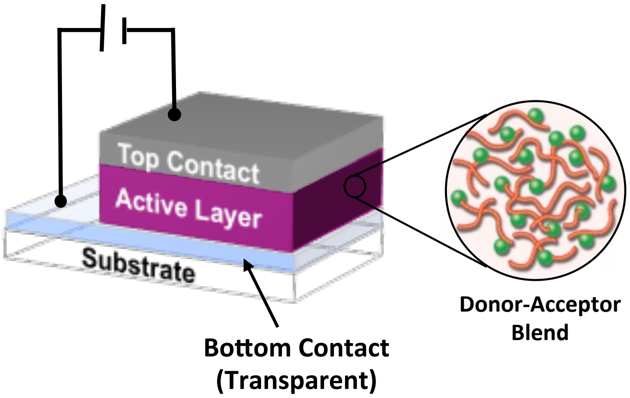

Fig. 1.1. Basic structure of an OPV cell

Another important difference to inorganic semiconductors lies in the orders of magnitudes lower charge-carrier mobility in organic semiconductors[21], which has a large effect on the design and efficiency of organic semiconductor devices. However, organic semiconductor have strong absorption coefficients ($\geq 10^5$ cm^{-1}), which partly balances low mobilities, giving high absorption in even <100nm thin devices[22].

In the simplest OPV cell architecture the active layer is in direct contact with both the anode and the cathode. This makes it possible for the acceptor material to transfer electrons to the hole-collecting anode, and vice versa, resulting in large leakage current, recombination, and decreased PV performance of the OPV[23]. To avoid leakage and improve charge collection, buffer layers are inserted to change the interface between active layers and electrodes. **Fig. 1.2** shows the structure of an OPV enhanced with both electron transport layer (ETL) and a hole transport layer (HTL). These layers adjust the energetic barrier height between the active layer and the electrodes, form a selective contact for carriers of one sort, set up the internal field, determine the polarity of the device, and sometimes act as optical spacer[16,24].

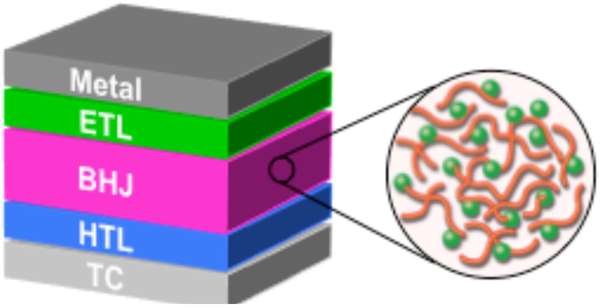

Fig. 1.2. Structure of an OPV cell with buffer layers

Although various materials such as MoO_3[25,26], WO_3[16,25], V_2O_5[27,28], NiO_x[29], and poly(3,4-ethylenedioxythiophene):poly(styrenesulfonate) (PEDOT:PSS) [16,30] have shown to be effective HTLs, and ZnO[31], TiO_2[30,32], LiF[33], Ca[34,35], and Ba[35] as ETLs, development of new materials suitable for low-temperature processing and large area deposition methods to be used as transport layer on OPVs are needed to compete with Si-based solar cells.

1.3 OPV Characterization

One of the primary ways to characterize a solar cell is by measuring current density as function of applied voltage in the dark and under illumination. The typical *J-V* characteristics of OPVs are shown in **Fig. 1.3**. To the left, the *J-V* curve of the cell in dark is shown. When a cell is illuminated, the *J-V* curve is shifted down by the short-circuit current density, J_{sc} (**Fig. 1.3**, right), which is the current density at zero bias.

The open-circuit voltage, V_{oc}, corresponds to the difference in the work functions of the metals and it balances the built-in field. The cell is placed in an open circuit and it is illuminated. Electrons and holes separate and flow towards the low and high work functions, respectively. At the same point the injected current equals the photocurrent. The square $J_{max}V_{max}$ is the maximum work the cell is able to yield. The fill-factor FF is a measure of closeness of the solar cell J-V curve to the rectangular shape (the ideal shape), and it is given by $J_{max}V_{max}/J_{sc}V_{oc}$. The PCE is defined by the power output delivered by the OPV divided by the incident light power[36].

$$PCE=V_{oc}\cdot J_{sc}\cdot FF/P_{in} \qquad \text{Eqn. 1}$$

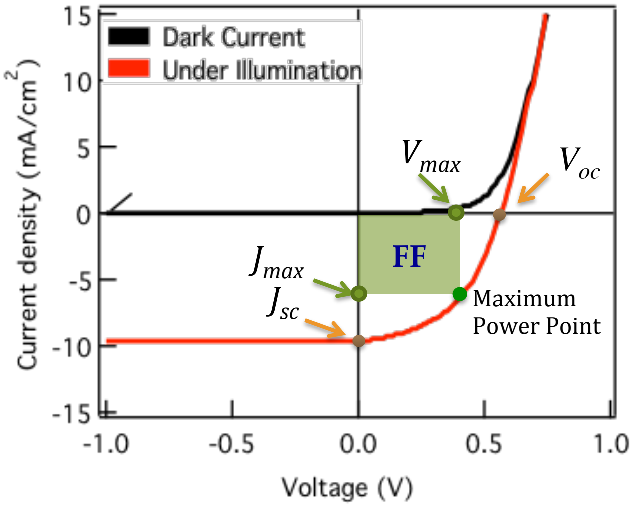

Fig. 1.3. *J-V* of an OPV cell under dark (black curve) and under illumination (red curve) conditions. The open circuit (V_{oc}) and short-circuit current density (J_{sc}) are shown. The maximum output is given by the square $J_{max}* V_{max}$.

In practice, solar cells can deviate from the ideal behavior predicted due to various reasons. The photogenerated charges have to travel through the semiconductor region to reach the respective electrode, which are thin and have an intrinsic resistance. This introduces an effective *series resistance* (R_{se}) into the photovoltaic circuit that generates a voltage drop and therefore prevents the ideal photovoltaic voltage from developing when a current is drawn. Besides the R_{se}, a fraction of the photogenerated carriers can also flow through the edges of the device or through grain boundaries instead of flowing through the external load. These effects prevent photogenerated carriers from flowing in the external circuit and are represented by an effective internal *shunt* or *parallel resistance* (R_{sh}) that diverts the photo current away from the load[37].

The R_{se} can significantly deteriorate the solar cell performance as shown in **Fig. 1.4a**, where $R_{se} = 0$ is the best solar cell case. It is clear how the available maximum power decreases with the series resistance, reducing the cell efficiency. Similarly, low R_{sh} values due to extensive defects in the material also reduce the efficiency (**Fig. 1.4b**).

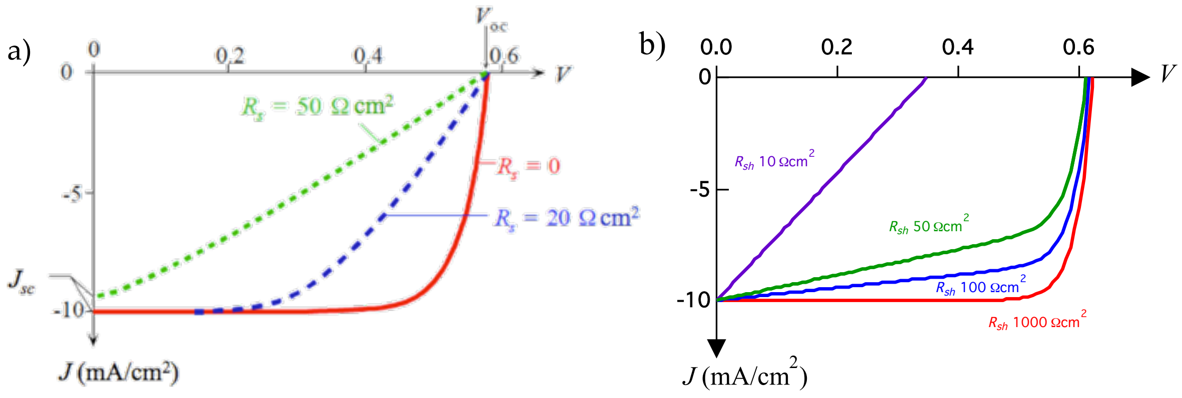

Fig. 1.4. Effect of the series resistance (a) and shunt resistance (b) on the solar cell efficiency

2 Hypothesis

The solution synthesis of *n*-type and *p*-type materials, such as metal oxides and transition metal dichalcogenides, will result in novel materials with electronic properties comparable to solution processed and vacuum deposited counterparts; thus, such properties combined with low-temperature deposition methods, makes them strong candidates for large-area films for electronic applications. The use of these materials as hole transport layer will exhibit excellent performance in organic photovoltaics, which will permit to reduce the time consumption and production costs compared with other fabrication techniques. Due to the simplicity and generality of the synthesis and deposition of these materials, the use of solution-processed methods will have a great potential for applications in many areas, such as photovoltaics, thin film transistors, batteries, and catalysis.

3 Objectives and Outlines

General Objective

The objective of this work is to improve of the OPV key parameters by using strategies to maximize every step on the working principles of the OPV cell. These include light absorption, exciton dissociation, free charges transport, and charge collection[20]. By maximizing every step enhancement of OPV overall performance is achieved. One route to improve the exciton dissociation is to investigate the effect of phase separation of the active layer caused by organic impurities on OPV overall performance. In addition, to develop new materials suitable for low-temperature processing and large area deposition methods to be used as transport layer on OPVs, enabling large area fabrication of OPVs.

Specific Objectives

- *Morphology of BHJ active layer.* To study the role of the surface chemistry of the underlying layer on the morphology of the BHJ active layer. By reducing the phase segregation of the active layer, an increase of interfacial area is obtained. This results in a drastic improvement of OPV parameters due to higher charge generation and lower bimolecular recombination[38].
- Synthesis of nanomaterial for large area deposition. The synthesis of material suspensions suitable for large area deposition, with

controlled size, stoichiometry, and electronic properties enabling a route towards low-cost OPV fabrication. The effect of synthesis conditions on the physical, chemical, and electric properties of these nanomaterials will be studied, and films casted from these suspensions will be used as transport layer for OPV.

- Solution processed transition metal dichalcogenides for electronic application. The synthesis and characterization of layered graphene-like materials, with electronic, optical, mechanical and thermal properties that makes them suitable for flexible electronic applications.

4 Characterization Techniques Applied

The following experimental techniques were employed in the proposed work to measure the corresponding properties of the materials:

- Scanning Kelvin Probe: work function measurements
- Photoelectron Spectroscopy in Air (PESA): ionization potential
- Ultraviolet Photoelectron Spectroscopy (UPS): work function and ionization potential measurements
- X-ray Photoelectron Spectroscopy (XPS): elemental composition
- Dynamic Light Scattering (DLS): nanoparticle hydrodynamic size
- Transmission Electron Microscopy (TEM): nanoparticle size, crystallinity
- Atomic Force Microscopy (AFM): surface morphology, work function (SKPM)
- Scanning Electron Microscopy (SEM): surface morphology
- UV-vis spectroscopy (UV-vis): optical bandgap, transparency
- Thermogravimetric Analysis: reaction temperature, reaction yield
- Fourier Transform Infra Red spectroscopy (FTIR): compound identification

The details of the instruments employed and the specific conditions of the measurements performed are explained in detail in further chapters.

5 Influence of ZnO sol-gel electron transport layer precursor processing on BHJ active layer morphology and OPV performance

Authors: Diego Barrera, Yun-Ju Lee, and Julia W.P. Hsu

Journal: Solar Energy Materials & Solar Cells, 125 (2014) 27-32.

5.1 Introduction

ZnO is a versatile semiconductor material, with wide range of applications in photoelectrochemical cells [39], lasers [40], and other electrical devices [41,42]. Due to its combination of low work function, large band gap, high crystallinity, and processability from precursor solutions [43,44], sol-gel ZnO films are frequently used as the electron transport layer in light emitting diodes [45,46] and organic photovoltaic (OPV) devices [31,47-53]. While ZnO nanoparticles or nanorods have been used for similar purposes [8], the performance of the these ZnO films depends strongly on the type and quantity of organic additives during synthesis [9] and post-processing steps [54,55]. Therefore, this paper will focus on forming ZnO films by sol-gel methods because they can be synthesized in one step and are widely used. Bulk heterojunctions (BHJs) consisting of blends of poly(3-hexylthiophene) (P3HT) and phenyl-C60-butyric acid methyl ester (PCBM) represent the best characterized active layer for OPV devices. In particular, thermal annealing of P3HT:PCBM BHJs has been shown to significantly improve all aspects of device performance [56], which is attributed to optimization of BHJ morphology such that the characteristic length of the P3HT:PCBM domains match the exciton diffusion length (~ 10 nm)

[18,57,58]. However, thermal annealing can create large (> 1 μm) clusters of crystalline PCBM [59,60], which were observed when using blends with high PCBM ratios [61,62] or when using long annealing times [63,64]. These clusters have been shown to lower OPV device performance due to decreased interfacial areas between P3HT and PCBM leading to poor charge collection [61-63,65]. Nevertheless, there has not been systematic studies on the influence of the underlying layer on the formation of PCBM clusters within the BHJ **Fig. 1.1**. In this report, we show that detailed processing of the sol-gel ZnO films can affect the area fraction of PCBM clusters upon thermal annealing and the OPV performance. In addition, we show that removal of residual organics after pyrolysis drastically reduces the formation of PCBM clusters and improves device performance, due to a reduction in bimolecular recombination as determined by white-light biased external quantum efficiency measurements [38].

5.2 Experiments

All chemicals were purchased from Fisher Scientific and were used as received unless otherwise noted. Inverted BHJ devices were fabricated on patterned indium tin oxide (ITO; 20 Ω/sq, Thin Film Devices). ZnO electron transport layer (ETL) was deposited in air using different approaches. For the first approach (MOE ZnO), 0.5M zinc acetate dihydrate and different concentrations of MEA ranging from 0.25M to 2M (default concentration = 0.5M) were dissolved in a 2-methoxyethanol (MOE) [44] and were spin-coated at 2000 rpm and pyrolyzed at 300 °C for 10 min. Following pyrolysis, some MOE ZnO films were rinsed with pure MOE spin-coated at 2000 rpm. For the second approach (EtOH ZnO), 0.053M zinc acetate dihydrate was dissolved in ethanol without a stabilizer, and two layers were spin-coated at 1000 rpm and pyrolyzed at 150 °C for 5 min [66]. For the BHJ, P3HT (RMI-001E, Rieke Metals, Inc.) and PCBM (Solenne BV) were dissolved in anhydrous chlorobenzene (Sigma-Aldrich) at a concentration of 25 mg/mL each, spin-coated at 1200 rpm, and annealed at 170 °C for 10 min in N_2 [9,67]. The thickness of active layer is approximately 200 nm. 5 nm MoO_3 hole transport layer (HTL) and 100 nm Ag electrode were thermally evaporated (Angstrom Engineering) to complete the devices, with area of 0.11 cm^2 each.

For FTIR measurements, ZnO films were deposited on 500μm *p*-type double-side polished Si(100) substrates (10-20 W cm, University Wafers). Absorbance spectra were taken at Brewster angle (θ =74°), using a Thermo Scientific Nicolet iS50 FTIR spectrometer with a mercury cadmium telluride detector (MCT). Thermogravimetric analyses (TGA) were done using a TA Instruments SDT Q600 thermogravimetric analyzer in the temperature range 20–600 °C with a heating rate of 1 °C/min, with 10 ml/min of air flux into alumina crucibles. UV-vis absorbance spectra were measured for ZnO films on glass using an Ocean Optics USB QE65 Pro spectrometer. Optical images were taken using a Leica DM2500M optical microscope, and were analyzed using ImageJ. The topography was studied using an Asylum MFP-3D atomic force microscope (AFM) under tapping mode. The current density-voltage (*J*-*V*) curves were measured in N_2 under a class AAA solar simulator (Sun 3000, Abet Technologies) with an AM 1.5G filter at 100 mW/cm^2 using a low noise source meter (2635A, Keithley). The simulator intensity was set using a NREL calibrated photodiode. For the white-light biased external quantum efficiency (EQE) measurements [68], the devices were placed in a o-ring sealed sample holder to avoid air exposure during the time of measurement (~1.5 hour). In brief, EQE spectra were taken using a chopped monochromated light (Horiba TRIAX-180, grating 600 groove/mm) from 350 to 750 nm with a wavelength window of 3.53 nm, while a white light emitting diode (MWWHL3, Thorlabs DC 2100) provided continuous background bias with intensity ranging from 1 to 100 mW/cm^2.

5.3 Results and Discussion

Fig. 5.1 shows the optical microscopy images of the surface morphology of annealed P3HT:PCBM deposited over ZnO films made by two different sol-gel recipes. P3HT:PCBM annealed on top of MOE ZnO contains a large number of objects with lateral dimensions of ~ 10 µm (**Fig. 5.1a**). The size and shape of these objects are consistent with PCBM clusters previously reported for P3HT:PCBM annealed at high temperature [62]. The cluster area fraction, defined as the area occupied by PCBM clusters divided by total area as determined from image analysis, is 0.33. In contrast, P3HT:PCBM annealed at the same temperature on top of EtOH ZnO contains a much lower number of clusters (**Fig. 5.1b**), with an area fraction of 2.4×10^{-3}. A similar reduction in the area fraction of PCBM clusters can be achieved if the MOE ZnO film is rinsed with MOE before BHJ deposition (**Fig. 5.1c**), with a cluster area fraction of 0.01. **Fig. 5.1d** shows a AFM image of a PCBM cluster found in **Fig. 5.1a**, which exhibits a height of 500 nm, approximately double the thickness of a typical P3HT:PCBM active layer. The presence of PCBM clusters suggests that the remainder of the BHJ has lower concentration of PCBM and probably a lower interfacial area between donor and acceptor. In addition, UV-vis spectroscopy showed increasing light scattering with PCBM cluster area fraction, indicating that high cluster area fraction BHJs have increased roughness, consistent with AFM data.

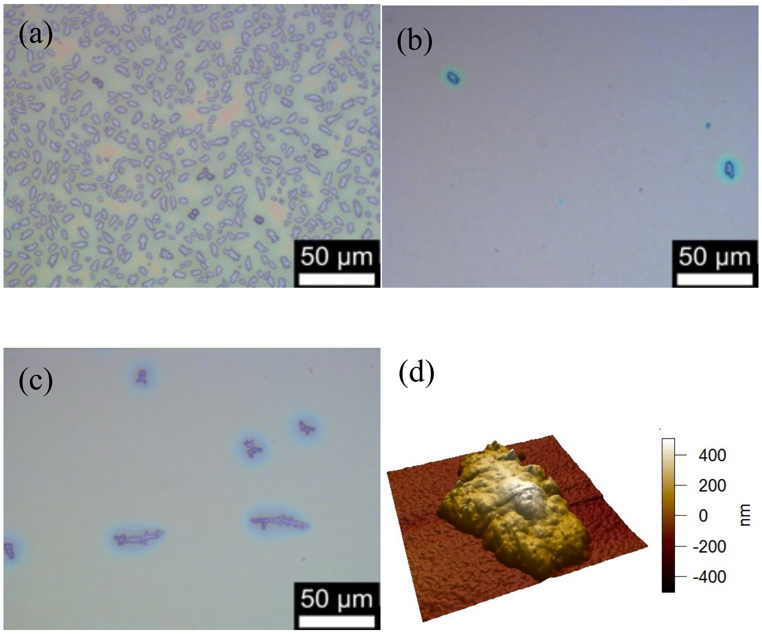

Fig. 5.1. Optical microscopic images of annealed P3HT:PCBM layer deposited on top of ZnO films made by (a) MOE ZnO, (b) EtOH ZnO, (c) rinsed MOE ZnO. (d) 5×5 μm AFM image of a typical PCBM sample.

Fig. 5.2 shows cluster area fraction of the P3HT:PCBM active layer annealed on top of the MOE ZnO films as a function of MEA concentration in the precursor solution ranging from 0.25M to 2M. The data show a strong correlation between the amount of MEA in the precursor and the formation of PCBM clusters. A saturation of the cluster area fraction near 0.50 can be seen, implying a virtually complete phase separation of P3HT and PCBM since the blend consists of 50% for each component. No data was shown for MEA concentrations below 0.25M because zinc acetate dihydrate did not fully dissolve at low stabilizer concentrations. Nevertheless, the ability to control cluster area fraction by varying MEA concentration allows us to systematically study the effect of cluster area fraction on device performance.

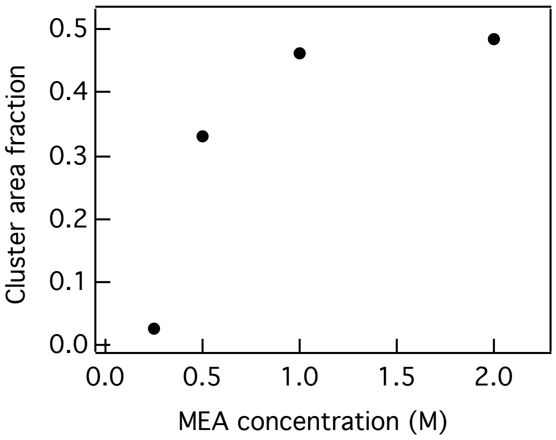

Fig. 5.2. Cluster area fraction vs MEA concentration in the precursor solution used to make MOE ZnO films, showing a positive correlation between the two parameters.

To understand the surface chemistry of MOE ZnO films, FTIR experiments were performed (**Fig. 5.3**). MOE ZnO before pyrolysis (**Fig. 5.3a**, black) shows peaks at 1590 cm^{-1} and 1425 cm^{-1}, corresponding to asymmetric and symmetric stretching vibration of C=O mode of zinc acetate [69]. The low energy C=O peak is superimposed with the stretching vibration mode of NH group present in MEA (~1420 cm^{-1}) [70], making a broad peak of organic species that include MEA. MOE ZnO after pyrolysis (**Fig. 5.3a**, blue, 45x amplitude) still exhibits both peaks, suggesting that most but not all of the organics were removed during pyrolysis at 300°C. The presence of residual organics after the 300 °C pyrolysis of zinc acetate-MEA based ZnO sol-gel films has been reported by Fujihara et al. [71], consistent with the TGA results (**Fig. 5.3b**) showing that weight loss continues up to 350 °C for complete decomposition of organics. However, annealing sol-gel ZnO on top of ITO up to 350°C leads to poor OPV performance due to ITO decomposition [72]. In comparison, MOE ZnO after 300°C pyrolysis and rinsing with MOE (**Fig. 5.3a**, green, 15x amplitude) shows no peaks near 1420 cm^{-1}, suggesting that MOE rinsing decreases residual organics level, most likely MEA, to below the detection limit of the MCT detector (~ 10^{-5}).

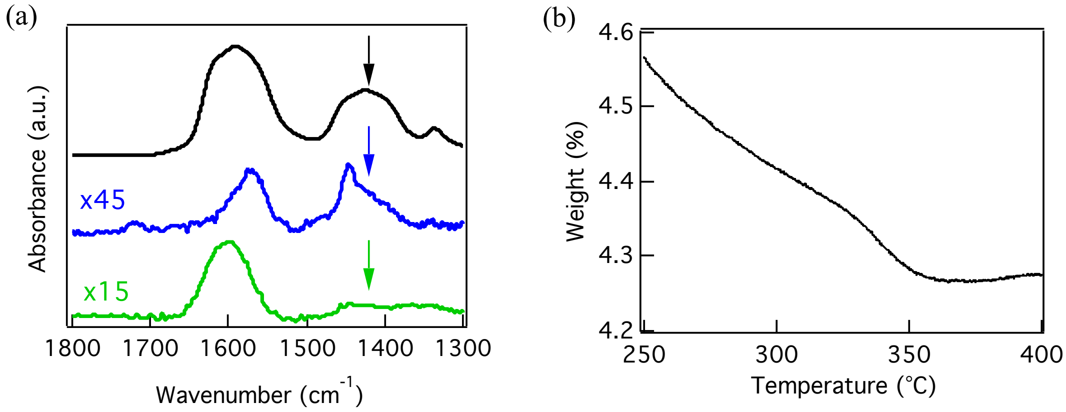

Fig. 5.3. (a) Comparison of FT-IR absorbance spectra for various MOE ZnO films: unpyrolyzed (black), pyrolyzed (blue, ×45), pyrolyzed and rinsed (green, ×15). The NH stretching mode at 1420 cm^{-1} is highlighted with an arrow. (b) TGA thermogram of MOE ZnO for temperature range 250– 400 °C.

Fig. 5.4 shows current density-voltage (*J-V*) characteristics at AM 1.5G 100 mW/cm^2 for devices made on top of MOE ZnO with cluster area fraction ranging from 0.01 to 0.46. Short circuit current density (J_{sc}), open circuit voltage (V_{oc}), fill factor (FF), and power conversion efficiency (PCE) values of these devices are summarized in **Table 5.1**. A clear reduction of performance in *J-V* curves of OPV devices as cluster area fraction increased can be seen. The black curve in

Fig. 5.4 is the device made on MOE ZnO ETL with rinsing to remove residual organics. The other devices are made on unrinsed MOE ZnO ETL. The performance of EtOH ZnO devices is similar to rinsed MOE ZnO devices. However, the EtOH ZnO ETL is less reliable due to poor stability of zinc acetate dehydrate in EtOH without a stabilizer, which limits maximum solubility to 0.053M and causes precipitation over a period of several hours, making it difficult to reproducibly deposit of a ZnO films with suitable thickness (~40 nm) without pinholes or aggregates. We found that PCBM clusters form in two regions: a low-density region with cluster area fraction ≤ 0.10 and a high-density region with cluster area fraction ≥ 0.30. In all devices used in this study (~ 120), we did not observe PCBM cluster area fraction between 0.10 and 0.30, indicating two different cluster formation mechanisms. In the low-density region, cluster formation was probably triggered by surface imperfections or dusts located randomly on the ZnO film (**Fig. 5.1b** and **Fig. 5.1c**). In the high-density region, the cluster formation arose from a much more uniform distributed source, possibly the residual organics (**Fig. 5.1a**). The gap between these two regions indicates an instability in the cluster formation.

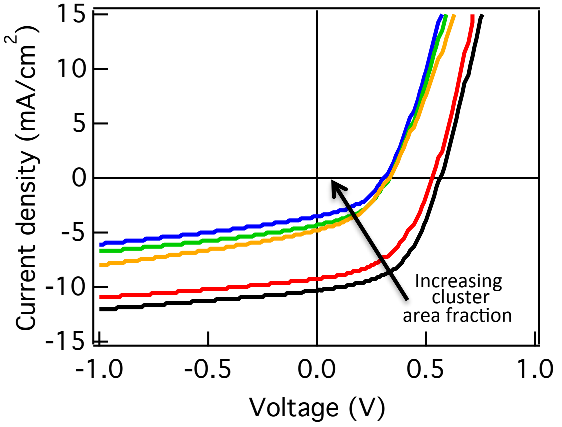

Fig. 5.4. Influence of cluster area fraction on *J-V* characteristics of solar cells under 100 mW/cm^2 AM 1.5G illumination.

Table 5.1. Summary of the device performance parameter dependence on cluster area fraction obtained from *J-V* characteristics of solar cells taken under 100 mW/cm^2 AM 1.5G illumination. Series resistance (R_{se}) and shunt resistance (R_{sh}) were calculated from *J-V* characteristics measured in the dark.

Cluster area fraction	V_{oc} (V)	J_{sc} (mA/cm^2)	FF ()	PCE (%)	R_{se} (Ω cm^2)	R_{sh} (Ω cm^2)
0.01	0.563 ± 0.005	10.32 ± 0.17	0.518 ± 0.022	3.01 ± 0.10	11 ± 2	5399 ± 476
0.06	0.532 ± 0.013	9.24 ± 0.33	0.474 ± 0.006	2.33 ± 0.16	9 ± 2	4807 ± 1631
0.34	0.328 ± 0.038	4.79 ± 0.89	0.402 ± 0.006	0.64 ± 0.21	19 ± 4	2871 ± 1173
0.39	0.330 ± 0.037	4.32 ± 0.92	0.424 ± 0.012	0.62 ± 0.22	14 ± 3	15088 ± 935
0.46	0.310 ± 0.014	3.51 ± 0.22	0.416 ± 0.015	0.45 ± 0.05	18 ± 4	4930 ± 1168

The dependence of J_{sc}, V_{oc}, FF, and PCE on cluster area fraction is depicted in **Fig. 5.5**. As noticed before, the dependence of device parameters on cluster area fraction can be divided into the same low and high cluster area fraction regions. Note that for cluster area fraction between 0.30 and 0.40, the results show larger standard deviation within a sample as well as sample-to-sample variation. This is consistent with cluster formation being unstable and minute differences leading to large variations in cluster area fraction. Despite some variations in the results, a clear trend is observed: the performance of the devices reflected on all four parameters decreases with increasing cluster area fraction. For cluster area fraction ≤ 0.1, the devices work well with average values of J_{sc}, V_{oc}, FF, and PCE of 9.7 ± 0.5 mA/cm^2, 0.55 ± 0.02 V, 0.47 ± 0.03, and 2.5 ± 0.3 %, respectively, over 25 devices. OPV device parameters with the cluster area fraction ≥ 0.3 show reductions of up to 45% in J_{sc}, up to 35% in V_{oc}, up to 15% in FF, and up to 65% in PCE compared to devices with cluster area fraction ≤ 0.1. Similar reductions in the OPV device parameters has been reported by van Bavel *et al.* for BHJ devices with PCBM clusters forming due to high PCBM concentrations [61], although their analysis is complicated by the effect of PCBM concentration on performance.

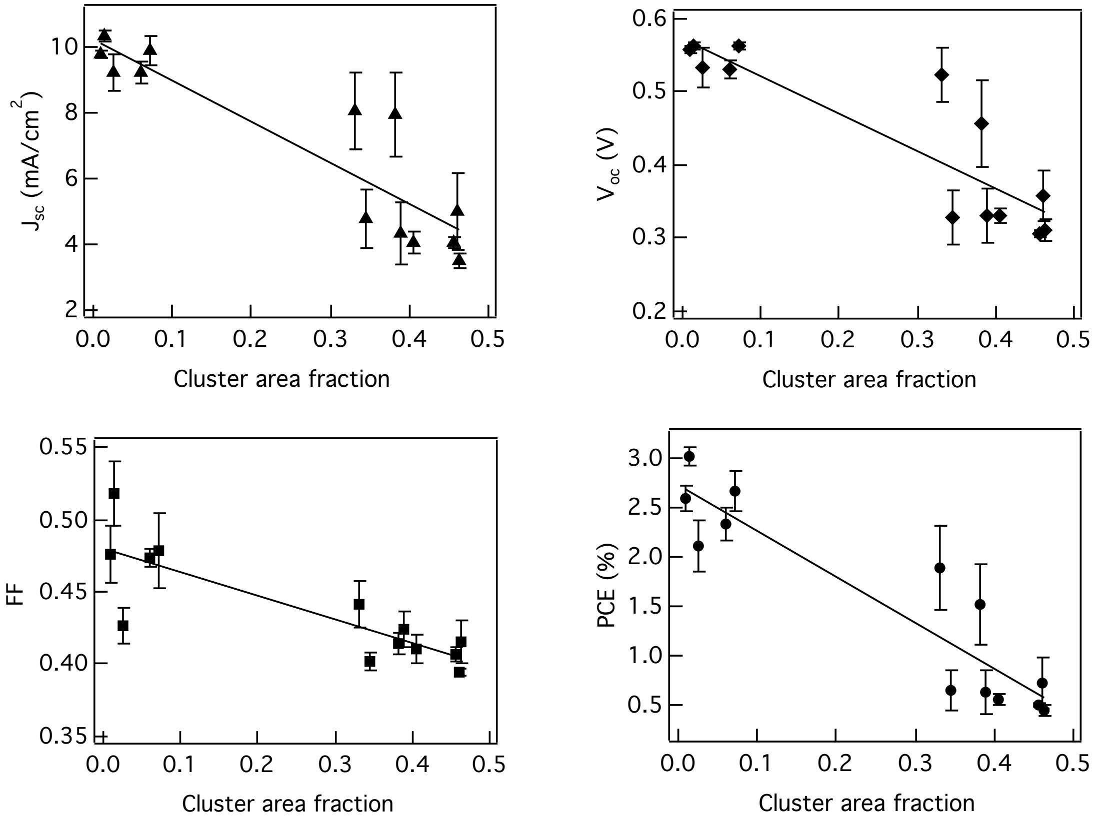

Fig. 5.5. Influence of cluster area fraction on OPV device parameters.

Fig. 5.6 shows J_{sc} values at 100 mW/cm^2 integrated from EQE spectra (J_{sc} *(EQE*)*) measured at different white-light bias intensities [38] for P3HT:PCBM devices on MOE ZnO with cluster area fraction of 0.01 (black, achieved by rinsing), 0.33 (red), and 0.46 (blue). J_{sc}*(EQE*)* represents the expected J_{sc} value of a device under AM1.5G 100 mW/cm^2 illumination for different levels of bimolecular recombination, which we control by varying the background white-light intensity and hence the carrier density inside the BHJ. It is evident that devices with high cluster area fraction (**Fig. 5.6**, red and blue) exhibit significantly lower J_{sc} *(EQE*)* compared to the device with low cluster area fraction

(**Fig. 5.6**, black) even at low background intensities, where bimolecular recombination is negligible, indicating that the presence of PCBM clusters in BHJs decreases carrier generation. This is likely caused by a lower degree of interpenetration between P3HT and PCBM. When $J_{sc}(EQE^*)$ at 100 mW/cm^2 background intensity is compared to the average value of J_{sc} (EQE^*) at low intensities (**Fig. 5.6**, dashed lines), a significantly greater reduction of performance is observed for devices with high cluster area fraction. For example, the device with 0.01 cluster area fraction exhibits a 2.6% decrease in $J_{sc}(EQE^*)$ at 100 mW/cm^2, while the devices with cluster area fractions of 0.33 and 0.46 exhibited decreases of 29% and 27%, respectively. This indicates that devices with high cluster area fraction experience higher bimolecular recombination, possibly caused by inefficient carrier transport in the non-aggregated regions of the active layer. We also found that after white-light biased EQE measurements, devices with high cluster area fraction degraded significantly, while devices with low cluster area fraction showed no significant change. Thus, low cluster area fraction in P3HT:PCBM BHJs, which can be achieved by rinsing the pyrolyzed MOE ZnO surface to remove residual organics (**Fig. 5.6** black), results in improved device performance both from increased charge generation and reduced bimolecular recombination.

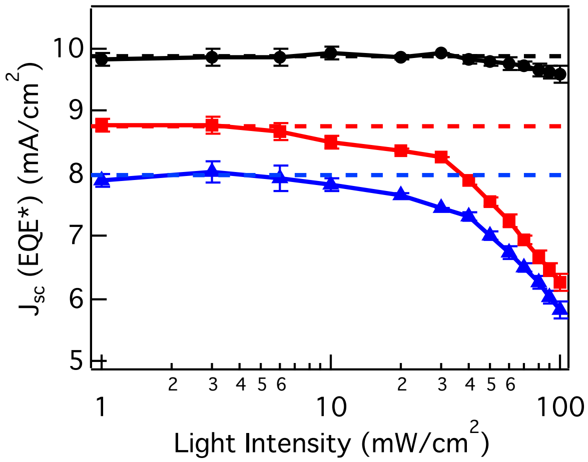

Fig. 5.6. Current density integrated from EQE spectra, J_{sc} *(EQE*)*, at different background intensities for P3HT:PCBM devices on MOE ZnO with cluster area fraction of 0.01 (black), 0.33 (red), and 0.46 (blue). Dashed lines represent average J_{sc} *(EQE*)* value at < 10 mW/cm^2 background intensity for each device.

5.4 Conclusions

In summary, we demonstrate the influence of the underlying layer on the BHJ layer morphology. We show that trace amount of organic species, possibly MEA, on the pyrolyzed MOE ZnO surface has a significant effect on the morphology of P3HT:PCBM BHJ films. When the active layer is deposited and annealed over a sol-gel ZnO ETL surface made from MEA containing precursor, PCBM clusters form during annealing, with cluster area fraction correlated with the MEA concentration in the precursor solution. This phase segregation leads to a reduction of interfacial area and lower PCBM concentrations outside of the clusters in the active layer, resulting in drastic reduction of OPV parameters due to both low charge generation and high bimolecular recombination. Rinsing the pyrolyzed MOE ZnO films with MOE or using a ZnO recipe without MEA significantly reduced the formation of PCBM clusters and produced devices with good performance.

6 In Situ Chemical Chemical Oxidation of Ultrasmall MoO$_x$ Nanoparticles in Suspension

Authors: Yun-Ju Lee, **Diego Barrera**, Kaiyuan Luo, and Julia W.P. Hsu

Journal: Journal of Nanotechnology, 195761 (2012).

6.1 Introduction

Metal oxide nanoparticles represent a large class of materials with applications in areas such as energy conversion and storage[20,73], catalysis[74,75], sensing[76], and biomedicine[77]. Major advantages of metal oxide nanoparticle suspensions include compatibility with low temperature, large area solution processing, versatile surface functionalization, and formation of complex architectures via self-assembly. Molybdenum oxide (MoO$_x$) has attracted much interest as a hole transport layer (HTL) material in organic light emitting diodes and solar cells because of its high work function (Φ). By matching Φ of the HTL to the highest occupied molecular orbital (HOMO) of the organic electron donor material[16], MoO$_x$ films inserted between the active layer and the anode has been shown to improve performance of organic photovoltaic (OPV) devices[13,23,27,50,78-81]. Most work in this area use thermally evaporated MoO$_x$ films[27,50,78,79]. While solution deposition of MoO$_x$ HTL films has been reported, all approaches thus far have required a post-deposition processing step that must be performed either at high temperature (≥ 160 °C) [23,80,81] and/or in an O$_2$-

containing ambient[13] to obtain MoO_x films with high Φ. In addition, the solvents currently used for the solution deposition of MoO_x do not wet the organic layer to form a uniform thin film as required in an inverted OPV architecture, which shows superior stability in air compared to conventional devices[82,83]. Recently, our group developed a microwave-assisted synthesis of MoO_x nanoparticles (npMoO_x) in n-butanol suspension, demonstrated formation of uniform thin films on poly(3-hexylthiophene):):[6,6]-phenyl-C61-butyric acid methyl ester (P3HT:PCBM) blends using room temperature solution processing, and examined performance of inverted OPV devices using npMoO_x films as HTLs[26]. Here we focus on *in situ* chemical oxidation to optimize the npMoO_x properties for HTL application. Specifically, we examined the effect of chemical oxidation conditions on the size and stability of the npMoO_x suspension to evaluate its suitability for the formation of uniform and pinhole free thin films. We also quantified the impact of chemical oxidation on Φ and stoichiometry MoO_x thin film, and demonstrated continuous tuning of Φ from 4.4 eV to 5.0 eV through precise control of the chemical oxidation conditions and Mo oxidation state. We show that *in situ* chemical oxidation of MoO_x nanoparticle is a versatile technique to synthesize stable suspensions of ultrasmall nanoparticles with desired stoichiometry and Φ for the formation of thin HTL on top of organic active layer without post processing.

6.2 Experiments

MoO_x nanoparticle ($npMoO_x$) suspensions were synthesized using nonhydrolytic sol-gel conversion of molybdenum dioxide bis(acetylacetonate) (Moacac) in anhydrous n-butanol as shown schematically in **Fig. 6.1**, following a microwave-assisted synthesis procedure modified from Bilecka and co-workers[84]. We selected this approach because it has been shown to yield various metal oxide nanoparticles with low size polydispersity, good stability, and short reaction times down to 3 min. Furthermore, the procedure does not require additional ligands for nanoparticle stabilization, and thus should allow the deposition of nanoparticle films with good carrier transport properties without the need to remove electrically insulating ligands through a post synthesis step. We used n-butanol as the solvent because of the good solubility for Moacac, and because it wets, but does not dissolve or swell, hydrophobic organic films such as P3HT:PCBM. For the microwave synthesis, a test tube of Moacac solution in n-butanol was mixed in N_2 and placed in a microwave reactor (CEM Discovery) containing a single mode 2.54 GHz microwave cavity. A Moacac concentration of 0.1 M was selected to balance complete dissolution and strong absorption microwave to enable rapid heating to 200 °C within three minutes. The Moacac solution was maintained at 200 °C for 15 min to synthesize the brown $npMoO_x$ suspension (**Fig. 6.1**). We chose to chemically oxidize $npMoO_x$ in suspension using H_2O_2 for three reasons: H_2O_2 is a strong oxidizing agent, H_2O_2 is miscible with n-butanol, and byproducts of the reaction, e.g. H_2O and O_2, can be easily removed during subsequent processing. For chemical oxidation, a small amount of 30 wt% H_2O_2 in H_2O (Fisher) was added to the npMoO$_x$ suspension to achieve the desired concentration (for example, 10.2 µL of 30 wt% H_2O_2 in H_2O per mL of suspension for 0.1 M H_2O_2). The mixture was then stirred at room temperature for times ranging from 20 min to 24 hr for oxidation to occur.

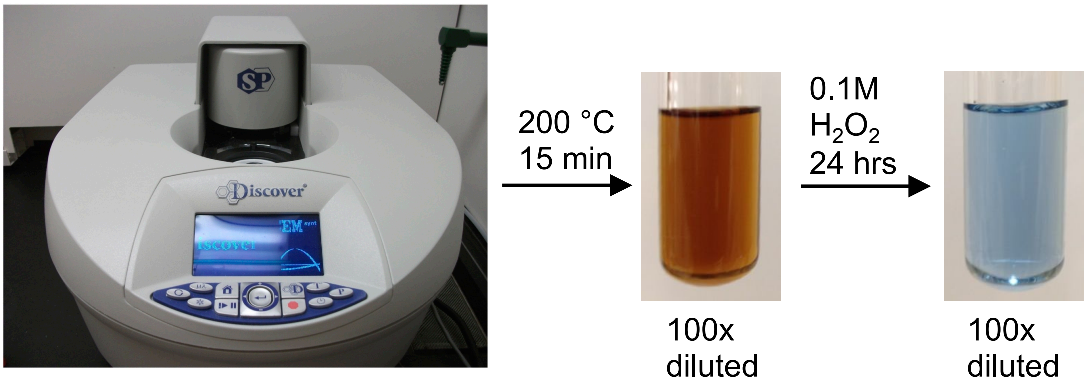

Fig. 6.1. Picture of microwave synthesis and chemical oxidiation of MoO$_x$ nanoparticles. A mixture of molybdenum oxide bis(acetylacetonate) in n-butanol was placed in a microwave reactor (CEM Discovery) and heated using 2.45 GHz radiation. When heated at 200 °C for 15 minutes, Moacac reacted, forming a brown suspension of nanoparticles. Chemical oxidation of the nanoparticle suspension with 0.1M H_2O_2 for 24 hours yielded a blue suspension of nanoparticles.

To determine the nanoparticle size and distribution, an aliquot of each npMoO$_x$ suspension was diluted by a factor of 10 with n-butanol, agitated in an ultrasonic bath (Branson) for 5 min, and passed through a 0.2 μm PTFE syringe filter. The diluted suspension was analyzed by dynamic light scattering (DLS) under backscattering conditions using a Malvern Zetasizer. To form thin films for these measurements, the npMoO$_x$ suspension without dilution was passed through a 0.2 μm PTFE syringe filter and spin coated at 1000 rpm on a cleaned ITO coated glass (20 Ω/□, Thin Film Devices). Φ of the MoO$_x$ film was measured using the Kelvin probe technique, and oxidation state of the Mo cation was determined using X-ray photoelectron spectroscopy (XPS). Φ of the npMoO$_x$ film was measured in air using an isoprobe electrostatic voltmeter (Model 244, Monroe Electronics), with Au as the reference material (Φ = 5.15 eV). XPS of the npMoO$_x$ film was carried out using a Perkin-Elmer 5600 ESCA system with monochromated Al KR source (1486.7 eV). All spectra were collected at an angle of 45° to the sample normal, with a pass energy of 58.7 eV and energy step of 0.125 eV. All XPS spectra were fitted using commercial software (MultiPak, PHI) and aligned to the C 1s reference at 284.8 eV. A reference sample of 20 nm MoO$_3$ on ITO was made by thermal evaporation at a rate of 0.1 A/s. A FWHM of 1.2 eV for each peak was used for peak fitting.

6.3 Results and Discussion

We found that microwave heating of Moacac resulted in a brown suspension of npMoO$_x$ (**Fig. 6.1**). Even without added ligands, the suspension showed excellent stability and remain dispersed for more than 90 days. DLS of the as-synthesized npMoO$_x$ suspension found a volume weighted mean diameter of 2.1 ± 0.9 nm (**Fig. 6.2a**, dashed line), in good agreement with the size determined using small-angle x-ray scattering (SAXS)[26]. Storage of the as-synthesized npMoO$_x$ in air for up to 120 hrs led to no change in size, as confirmed by DLS (data not shown). In contrast, we found that chemical oxidation with H_2O_2 modified the size of the resulting nanoparticles in a complex way (**Fig. 6.2a**). For example, 0.1M (**Fig. 6.2a**, blue) and 0.3M (**Fig. 6.2a**, red) H_2O_2 at short reaction times ranging from 20 min to 3 hr decreased the npMoO$_x$ diameter to ~ 1 nm. In comparison, a further increase in reaction time to 24 hr caused the nanoparticle size to increase back to 2 nm. The increase in size with longer reaction time is consistent with our previous observation that the average diameter of chemically oxidized npMoO$_x$ from SAXS had increased to 4 nm after ~ 15 days of chemical oxidation[26], and indicates that Ostwald ripening for these nanoparticles only occurs with the addition of H_2O_2. Nevertheless, the nanoparticles are still small enough to form multilayer films with thickness of ~ 10 nm. Indeed, we previously showed using atomic force microscopy that a chemically oxidized MoO$_x$ suspension spin coated on top of P3HT:PCBM formed a pinhole-free film that planarized the roughness of the underlying P3HT:PCBM layer[26]. Thus, while npMoO$_x$ size increases after chemical oxidation with H_2O_2, it remains sufficiently small to form uniform films on top of organic layers at thickness values that are relevant for HTL in OPV devices.

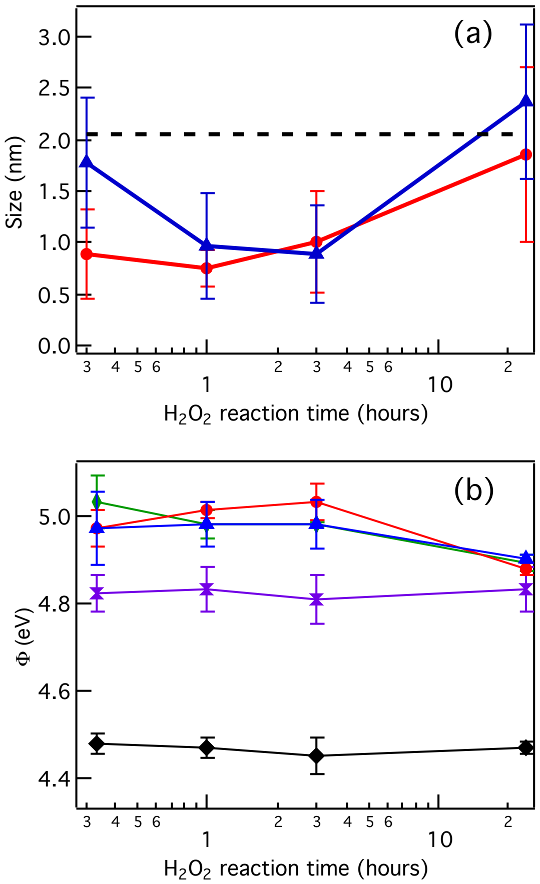

Fig. 6.2. Effect of chemical oxidation with H_2O_2 on MoO_x nanoparticle properties. a) Dependence of nanoparticle size on chemical oxidation time (up to 24 hrs), showing that compared to as-synthesized nanoparticles (dashed line), both 0.1M H_2O_2 (blue) and 0.3M caused npMoO_x size to decrease to 1 nm (up to 3 hrs) and then increase back to 2 nm (24 hr). b) Dependence of nanoparticle film Φ versus chemical oxidation conditions, showing Φ of as-synthesized npMoO_x (black) was increased from 4.48 eV to 4.85 eV with 0.05M H_2O_2 (purple) and that the increase was independent of the reaction time between 20 min and 24 hr. In contrast, 0.1M (blue), 0.2M (green), and 0.3M (red) H_2O_2 all caused work function to increase to 5.0 eV with a reaction time of

up to 3 hr. However, a further increase in reaction time to 24 hrs decreased Φ to 4.9 eV.

Chemical oxidation of the MoO_x nanoparticles significantly altered the electronic properties of $npMoO_x$ films, as measured by their Φ values in air. The as-synthesized $npMoO_x$ films exhibited a low Φ of 4.48 ± 0.02 eV. Addition of 0.05M H_2O_2 for 20 min caused Φ to increase to 4.82 ± 0.04 eV, and longer reaction times did not significantly increase Φ (**Fig. 6.2b**, purple). Increasing H_2O_2 concentration to 0.1M and above caused Φ to increase to 4.94 ± 0.01 eV after 1 hr, and the value remained unchanged when increasing the reaction time to 3 hr (**Fig. 6.2b**). However, a further increase in reaction time to 24 hr caused Φ to decrease to 4.90 ± 0.01 eV. We note that the decrease in Φ corresponded to the change of the nanoparticle suspension color from brown to blue (**Fig. 6.1**).

To quantitatively understand the origin of the change in Φ with chemical oxidation, we examined the stoichiometry of $npMoO_x$ films with different H_2O_2 reaction conditions using XPS. As a reference, we measured an evaporated MoO_3 film and found that the Mo 3d XPS spectra can be fitted to doublet peaks at 232.3 eV and 235.4 eV, corresponding to Mo $3d_{5/2}$ and Mo $3d_{3/2}$ peaks for Mo^{6+}, plus very weak doublet peaks at 231.0 eV and 233.8 eV corresponding to Mo $3d_{5/2}$ and Mo $3d_{3/2}$ peaks for Mo^{5+}[26,84,85]. The Mo^{6+} fraction, defined as the area under the Mo^{6+} peaks divided by the total peak area, was 0.95, indicating that the reference sample was almost pure MoO_3. The FWHM of the fitted peaks was 1.2 eV, and this value was used for all peaks when fitting XPS spectra of $npMoO_x$ films where there are significant contributions to the overall signal from multiple oxidation states, in order to quantify the atomic fraction from each oxidation state. For example, the Mo 3d XPS spectra of as-synthesized $npMoO_x$ contain peaks at 232.4 eV and 235.5 eV from Mo^{6+}, 231.4 eV and 234.5 eV from Mo^{5+}, and 229.8 eV and 232.9 eV from Mo^{4+} (**Fig. 6.3a**). The Mo^{6+} fraction was 0.21, showing that as-synthesized $npMoO_x$ is mostly reduced. Reaction with 0.05M H_2O_2 for 1 hr caused the Mo^{6+} peaks to increase in intensity at the expense of the Mo^{5+} and Mo^{4+} peaks, (**Fig. 6.3b**), so that the Mo^{6+} fraction increased to 0.60. Nevertheless, the XPS spectra clearly show that 0.05M H_2O_2 only partially oxidized the as synthesized MoO_x nanoparticles to MoO_3. Increasing the H_2O_2 concentration to 0.1M resulted in Mo 3d XPS spectra consisting almost entirely of peaks at 232.6 eV and 235.7 eV from Mo^{6+}, with a miniscule contribution from Mo^{5+} peaks at 230.9 eV and 234.1 eV (**Fig. 6.3c**). The corresponding Mo^{6+} fraction of 0.97 indicates that 0.1M H_2O_2 for 1 hr oxidized $npMoO_x$ to the extent similarly to the evaporated MoO_3 film. Increasing the reaction time to 24 hr at 0.1M H_2O_2 caused the Mo^{5+} and Mo^{4+} peaks to reappear in the Mo 3d XPS spectra (**Fig. 6.3d**), decreasing the Mo^{6+} fraction to 0.55. We believe the partial reduction of $npMoO_x$ with increased H_2O_2 reaction time can be explained by the electrochromism of MoO_3. MoO_3 is known to change to a blue coloration upon the insertion of small cations such as H^+, following the reaction[86]

$$MoO_3 + xH^+ + xe^- \rightarrow MoO_{3-x}(OH)_x \qquad \text{Eqn. 2}$$

In our case, H^+ is supplied by the H_2O in the 30 wt% H_2O_2 solution, and e^- may be supplied by oxidation of neighboring Mo^{4+} and Mo^{5+} atoms. This reaction scheme is consistent with the observation that the change in npMoO$_x$ coloration from brown to blue was only observed after 24 hr reaction with 0.1M and 0.3M H_2O_2. The onset of color change, and by reference the proton insertion, also coincides with the increase in nanoparticle size and reduction in Φ. Thus, analysis of XPS spectra reveals that chemical oxidation with H_2O_2 consists of two concurrent processes, a fast oxidation that is complete at 0.1M and higher H_2O_2 concentrations within ~ 1 hr, and a slow reduction caused by H^+ insertion that occurs after ~ 24 hr, highlighting the importance of the chemical oxidation conditions on the stoichiometry of the resulting npMoO$_x$.

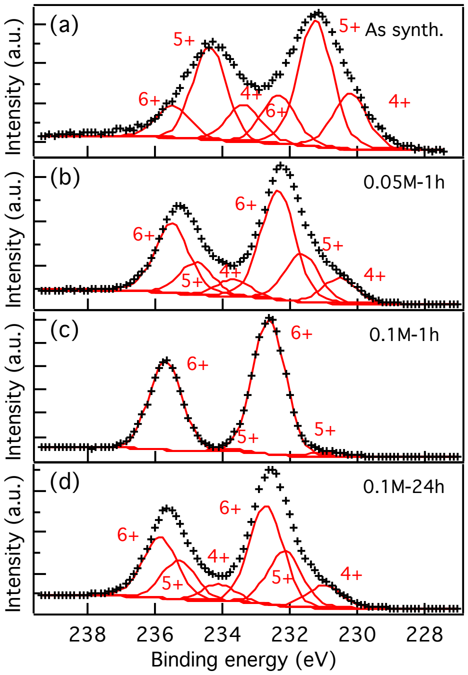

Fig. 6.3. Effect of chemical oxidation conditions on MoO_x nanoparticle stoichiometry. a) Mo 3d XPS spectra of as-synthesized $npMoO_x$ on ITO (crosses) and curve fit (solid), showing mixed oxidation states with contributions from Mo^{5+}, Mo^{4+}, and a small amount of Mo^{6+}. b) Mo 3d XPS spectra of $npMoO_x$ after chemical oxidation with 0.05M H_2O_2 for 1 hr, showing mixed oxidation states with a majority of Mo^{6+} oxidation state. c) Mo 3d XPS spectra of $npMoO_x$ after chemical oxidation with 0.1M H_2O_2 for 1 hr, showing almost complete oxidation to Mo^{6+} oxidation state. d) Mo 3d XPS spectra of $npMoO_x$ after chemical oxidation with 0.1M H_2O_2 for 24 hr, showing mixed oxidation states with a majority of Mo^{6+} oxidation state.

Fig. 6.4 depicts Φ and Mo^{6+} fraction that can be achieved using the *in situ* H_2O_2 chemical oxidation approach. For npMoO$_x$ films that were chemically oxidized at different H_2O_2 concentrations for 1 hr (**Fig. 6.4**, circles) and at 0.1M H_2O_2 for 24 hr (**Fig. 6.4**, triangle), the data show a strong correlation between the two parameters, suggesting that a clear relationship exists between MoO$_x$ nanoparticle stoichiometry and electronic properties. A continuous tuning of the Mo^{6+} fraction between 0.2 and 1.0, and Φ from 4.4 eV to 5.0 eV was achieved. Such control should allow us to systematically study the effect of MoO$_x$ composition on device performance in various applications.

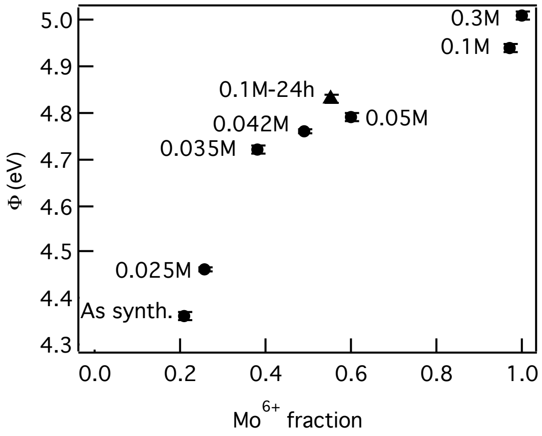

Fig. 6.4. Φ versus Mo^{6+} fraction for npMoO$_x$ as synthesized and chemically oxidized at 0.025M, 0.035M, 0.042M, 0.05M, 0.1M, and 0.3M H_2O_2 concentrations for 1 hr (circles) and at 0.1M H_2O_2 for 24 hour (triangle), showing a positive correlation between the two parameters.

6.4 Conclusions

In conclusion, through a systematic study of the effect of H_2O_2 concentration and reaction time on nanoparticle size, work function, and stoichiometry, we demonstrate that *in situ* chemical oxidation of MoO_x nanoparticle suspensions with H_2O_2 is a simple but versatile method to control their stoichiometry and electronic properties. Starting from suspensions of ultrasmall (d ~ 2 nm) MoO_x nanoparticles in n-butanol synthesized by a one-step microwave heating procedure, we found that short time (≤ 3 hr) reactions at room temperature with sufficiently high (≥ 0.1 M) concentration of H_2O_2 result in ≤ 1 nm MoO_x nanoparticles with high work function and almost entirely MoO_3, properties which are desirable for HTL material in OPV devices. However, long chemical oxidation times (≥ 24 hr) increase nanoparticle size and reduce Mo oxidation state and film's work function. By comparing Kelvin probe results and XPS spectra of npMoO_x films that have been chemically oxidized under various conditions, we established a clear correlation between the work function and the Mo^{6+} fraction of the npMoO_x, and achieved a continuous tuning of work function values from 4.4 to 5.0 eV and Mo^{6+} fraction from 0.2 to 1.0. Such precise control of MoO_x stoichiometry and properties is crucial for the optimization of npMoO_x as a solution processible material for various applications. Moreover, the simplicity of the chemical oxidation procedure should be generally applicable in synthesizing other transition oxide nanomaterials with tunable stoichiometry and properties.

7 General Method to Synthesize Ultrasmall Metal Oxide Nanoparticle Suspensions for Hole Contact Layers in Organic Photovoltaic Devices

Authors: Yun-Ju Lee, **Diego Barrera**, Jian Wang, and Julia W.P. Hsu

Journal: MRS Communications, (2015).

7.1 Introduction

Thin films of semiconducting metal oxides are frequently used to modify the interfaces organic semiconductor devices due to the large variety of materials with well-characterized optical and electronic properties and good chemical and physical stability[87]. Metal oxide films deposited from nanoparticle (NP) suspensions in theory combine the properties of metal oxides with large-area and low-temperature processing, which improves compatibility with organic devices but also create processing challenges. For example, organic photovoltaics (OPVs) represent a promising route toward low-cost, lightweight renewable energy generation[88,89]. Contact layers between bulk heterojunction (BHJ) active layers and electrodes can significantly improve performance of OPVs[16]. To fully realize the potential benefits of vacuum-free processing for low-cost OPVs, solution processed contact layers are intensively researched in recent years[7,88-90]. Various solution processed metal oxide films with high work function Φ have been utilized as hole contact layers (HTLs) in OPVs, which exhibit higher open circuit voltage V_{oc}[91], higher fill factor FF[7,14,23,91-94], and improved device stability[92,93] compared to the well-established conducting polymer (poly(3,4-ethylenedioxythiophene):poly(styrene sulfonate) (PEDOT:PSS) HTL.

Despite the recent progress, the stringent processing requirements of organic semiconductor devices have prevented general adoption of solution processed metal oxide films as interfacial layers. For example, published reports on solution processed metal oxide NP films as HTLs in OPVs typically require harsh post-deposition treatments, including annealing at temperatures > 100 °C[23,81,91-98], annealing for hours to days[14,28], and O_2 plasma treatment[91,96,97], all of which decrease compatibility with organic devices. We previously reported *in situ* oxidation of MoO_x NPs in n-butanol to MoO_3 with H_2O_2, but Φ after oxidation was still 0.3 eV lower than evaporated MoO_3 films[26]. Alternatively, NP suspensions have been formed by dispersing metal oxide NP powders in alcohols with ultrasonication[99], but this approach is limited by the availability of the powders and by NP size, typically > 10 nm. Also, with a few notable exceptions[91,95], most publications on solution processed metal oxide NP HTLs have focused on *n*-type NPs[14,23,26,28,81,92-94,96-99]. Here, we demonstrate a general method to synthesize suspensions of ultrasmall (1-2 nm) MoO_3, WO_3, NiO_x, and CoO_x NPs in n-butanol. Spin coated metal oxide NP films with no post-deposition treatment exhibit high Φ and ionization energy IE comparable to vacuum deposited films and consistent with the oxidation states of the metal cations. Finally, we examine the performance these NP films as HTLs in conventional poly[N-9'-heptadecanyl-2,7-carbazole-alt-5,5-(4',7'-di-2-thienyl-2',1',3'-benzothiadiazole)]:phenyl-C_{71}-butyric acid methyl ester

($PCDTBT:PC_{71}BM$) OPVs.

7.2 Experiments

Metal oxide NP synthesis and characterization: metal oxide NP suspensions in n-butanol were synthesized using a modified version of a published recipe[100]. Mo (average particle size 2-4 μm), W (1-5 μm), Ni (2.2-3.0 μm), and Co (1.6 μm) powders were purchased from Alfa Aesar and were used as received. In a typical reaction, 0.3 mmol metal powder was added to 525 μL n-butanol (Fisher) and 75 μL HCl (37% in H_2O, Fisher) and stirred at 25 °C for 20 min. 2220 μL of n-butanol and 180 μL of H_2O_2 (30% in H_2O, Fisher) were then added, and the solution was stirred at 25 °C for 16 hr, yielding 0.1M suspension of metal oxide NPs. The product was passed through a 0.2 μm PTFE syringe filter (Pall), and was used without further purification. DLS was performed using a Malvern ZetaSizer Nano ZS. For TEM, NiO_x NP suspension was diluted to 0.005M with n-butanol, drop casted on a TEM grid (01824, Ted Pella), and imaged at 200 kV with a JEOL JEM2100. NP diameter was analyzed using ImageJ and represents an average of 80 NPs. Metal oxide NP films of different thicknesses were formed by diluting the stock NP suspensions with n-butanol, and spin coating 2-4 layers. For Φ and XPS measurements, 0.05M metal oxide NP suspensions were spin coated twice at 8000 rpm on unpatterned ITO on glass (20 Ω/□, Thin Film Devices) that had been cleaned by rinsing with IPA and H_2O, follow by UV-O_3 cleaning for 20 min (BioForce Nanosciences). Φ was measured in air using a scanning

Kelvin probe (SKP 5050, KP Technology), with Au as the reference material (Φ = 5.15 eV). XPS was measured using a Ulvac-PHI VersaProbe 2 with monochromated Al Kα source (1486.8 eV). All spectra were collected at an angle of 45° to the sample surface with energy step of 0.1 eV and pass energy of 23.5 eV, and were fitted using commercial software (MultiPak, Ulvac-PHI). UPS was measured on MoO_3 and WO_3 films using the same instrument with He I plasma source (21.2 eV) with energy step of 0.1 eV. PESA was performed on NiO_x and CoO_x NP films using a RKI Instruments Model AC-2 system with 100 nW deuterium lamp power and energy scanning between 4.8 eV and 6.2 eV with a step of 0.05 eV. The standard deviation for Φ measurement was found to be 0.03 eV. The uncertainty of the UPS and PESA measurements were found to be 0.1 eV and 0.05 eV, respectively.

OPVs fabrication and characterization: Conventional PCDTBT:$PC_{71}BM$ OPVs were fabricated following published procedure[101] with modifications. Metal oxide NP suspensions (0.025M for MoO_3, 0.00625M for others) were spin coated four times at 8000 rpm on patterned ITO on glass (20 Ω/□, Thin Film Devices) to form the HTL. For reference devices, PEDOT:PSS (Clevios P VP AI 4083, Heraeus) was mixed with isopropanol in a 7:3 volume ratio, spin coated at 4000 rpm on patterned ITO, and annealed in N_2 at 170 °C for 5 min to form the HTL. PCDTBT (1-Material) and $PC_{71}BM$ (Solenne BV) were dissolved at 7:28 mg/mL in ortho-dichlorobenzene (Aldrich), spin coated at 2000 rpm, and annealed in N_2 at 70 °C for 15 min to form 50 nm thick BHJ. Finally, Ca (7 nm) and Al (150 nm) were thermally evaporated (Angstrom Engineering) to complete the devices. The class AAA solar simulator (Sun 3000, Abet Technologies) contained AM1.5G filter, with the intensity adjusted to 100 mW/cm^2 using a calibrated Si photodiode with KG5 filter (RR_227 KG5, Abet Technologies). J-V measurement was performed in N_2 using a low noise sourcemeter (2635A, Keithley) controlled by LabView (National Instruments). A 2.5 mm diameter aperture was placed in front of each device to rigorously define the illumination area to 0.049 cm^2. All data shown represent the average of at least five devices.

7.3 Results and Discussion

7.3.1 NP and Film Properties

The metal oxide NP suspensions were synthesized by controlled oxidative dissolution of micron-sized metal powders in the presence of H_2O_2 and HCl, using a modification of published procedure[100]. We found that by replacing the original solvent of water with n-butanol, and by reducing the metal concentration to 0.1M, the diameter of the dispersed NPs measured using dynamic light scattering (DLS) was reduced from ~ 5 nm to 0.7 ± 0.1 nm, 1.6 ± 0.4 nm, 1.0 ± 0.2 nm, and 0.9 ± 0.4 nm for MoO_3, WO_3, NiO_x, and CoO_x respectively (**Table 7.1**). The surfactant-free NP suspensions exhibit different colors arising from bandgap and/or intraband d-d transitions of the metal oxides (**Fig. 7.1b** inset), and remain dispersed without change in DLS size for at least two weeks. **Fig. 7.1a** depicts a typical transmission electron microscopy (TEM) image of NiO_x NPs, showing spherical particles with diameter of 1.3 ± 0.7 nm, consistent with the DLS result. High magnification image of a single NiO_x NP gives a characteristic spacing of 0.24 nm (**Fig. 7.1a**, inset), which matches the spacing from (111) planes of NiO. Thus, oxidation of metal powder by H_2O_2 in n-butanol produces stable suspensions of ultrasmall metal oxide NPs.

Table 7.1. Properties of metal oxide NP suspensions and films.

Material	Diameter[a] (nm)	Φ (eV)	IE (eV)
MoO_3 NP	0.7 ± 0.1	5.20	8.55[b]
WO_3 NP	1.7 ± 0.4	5.31	8.23[b]
NiO_x NP	1.0 ± 0.2	5.11	5.55[c]
CoO_x NP	0.9 ± 0.4	5.16	5.70[c]

[a] Measured in suspension by DLS
[b] Measured by UPS
[c] Measured by PESA

Metal oxide NP films spin coated on ITO were characterized in air unless otherwise noted to examine their electronic properties. Φ was measured using a scanning Kelvin probe, and was found to be 5.20 eV for MoO_3, 5.31 eV for WO_3, 5.11 eV for NiO_x, and 5.16 eV for CoO_x (**Table 7.1** and **Fig. 7.1b**). These values are significantly higher than bare ITO (4.85 eV) and PEDOT:PSS (4.95 eV), and is consistent with film thickness of ~ 5 nm measured by spectroscopic ellipsometry. The Φ values are similar to published data for solution processed NP films of MoO_3[102], WO_3[97], and NiO_x[95]; Φ for CoO_x NP film has not been reported. The ~ 1 eV decrease in Φ compared to vacuum deposited films[103] is probably caused by adsorption of hydrocarbon species[102] due to solution processing. The Φ and ellipsometry data suggest that spin coating results in significant coverage of the ITO surface with metal oxide NPs.

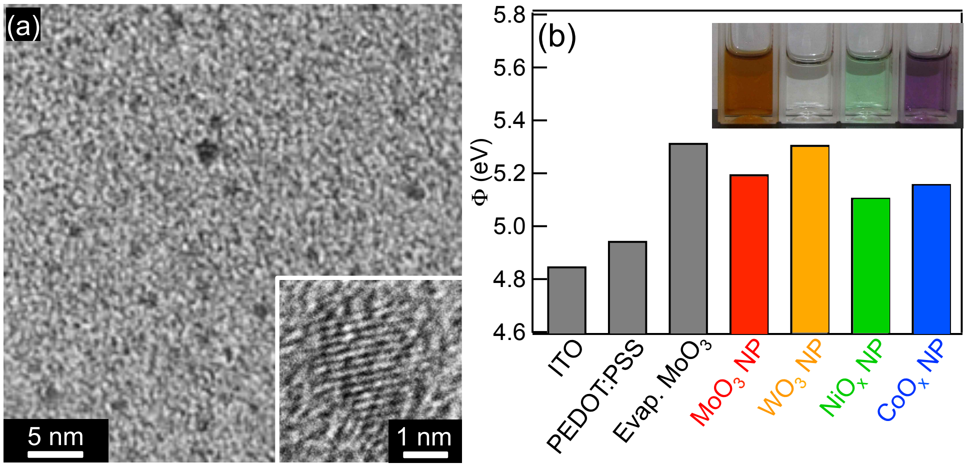

Fig. 7.1. (a) TEM images of NiO_x NPs. Inset: high magnification image of single NP, showing lattice spacing of 0.24 nm. (b) Φ values for ITO and various films on ITO. The error bar for Φ measurement is 0.03 eV.

IE of MoO_3 and WO_3 NP films was measured by UPS, yielding values of 8.6 eV and 8.2 eV, respectively (**Table 7.1**). These two oxides' IE cannot be measured by photoelectron spectroscopy in air (PESA), due to the upper limit of the deuterium source (6.2 eV). MoO_3 and WO_3 NPs exhibit bandgap 2.95 eV and 3.45 eV, respectively, as measured by UV-vis absorbance spectroscopy, in good agreement with literature[87]. In other words, Φ is similar to electron affinity EA (EA = IE – E_g), and these oxides are *n*-type. For NiO_x and CoO_x NP films, IE measured by PESA is 5.55 eV and 5.70 eV, respectively (**Table 7.1**). Given bandgaps from literature for NiO_x (3.7 eV)[29] and CoO (2.4 eV)[87], we see that Φ is similar to IE, suggesting that they are *p*-type. The IE values are consistent with published results on MoO_3[80] and NiO_x[29]

NP films, while IE values for solution processed WO_3 and CoO_x NP films have not been reported. In summary, the electronic levels of our solution processed metal oxide NP films are comparable to solution processed and vacuum deposited films of both *n*-type and *p*-type semiconductors, without the need for post-deposition treatment.

The stoichiometry of metal oxide NP films on ITO was characterized by x-ray photoelectron spectroscopy (XPS). The Mo 3d spectra can be fitted to doublet peaks at 232.4 eV and 235.6 eV with the same FWHM and 3:2 areal ratio (**Fig. 7.2a**), corresponding to Mo $3d_{5/2}$ and Mo $3d_{3/2}$ peaks of pure MoO_3. Similarly, the W 4f spectra can be fitted to doublet peaks at 35.7 eV and 37.8 eV with the same FWHM and 4:3 areal ratio (**Fig. 7.2b**), corresponding to W $4f_{7/2}$ and $4f_{5/2}$ peaks of pure WO_3. The Ni $2p_{3/2}$ spectra contains peaks at 855.4 eV, 860.9 eV, and 864.1 eV (**Fig. 7.2c**), corresponding to either NiO or $Ni(OH)_2$[104,105]. In addition, the peak at 857.3 eV matches NiOOH previously reported for post processed NiO_x NP film[105]. The O 1s spectra shows peaks at 529.2 eV, 530.5 eV, and 531.7 eV, confirming the presence of NiO, $Ni(OH)_2$, and NiOOH, respectively[105]. The NiOOH was previously shown to establish a surface dipole which increases Φ and IE of post processed NiO_x NP films[105], and may play a similar role in our films. The Co $2p_{3/2}$ spectra contains peaks at 780.4 eV, 782.2 eV, and 786.4 eV (**Fig. 7.2d**), corresponding to CoO or $Co(OH)_2$[104]. In addition, a weak peak at 785.0 eV may correspond to Co_3O_4, although unambiguous assignment is difficult due to the complex surface chemistries of CoO_x and the resulting overlap in XPS peaks[104]. The O 1s spectra shows peaks at 529.6 eV, 531.0 eV, and 532.7 eV, corresponding to CoO, $Co(OH)_2$, and adsorbed H_2O, respectively[104].

Thus, as deposited metal oxide NP films show stoichiometric MoO_3 and WO_3, and mixed NiO_x and CoO_x. The high oxidation states of the metal cations are consistent with the high Φ of the NP films[103].

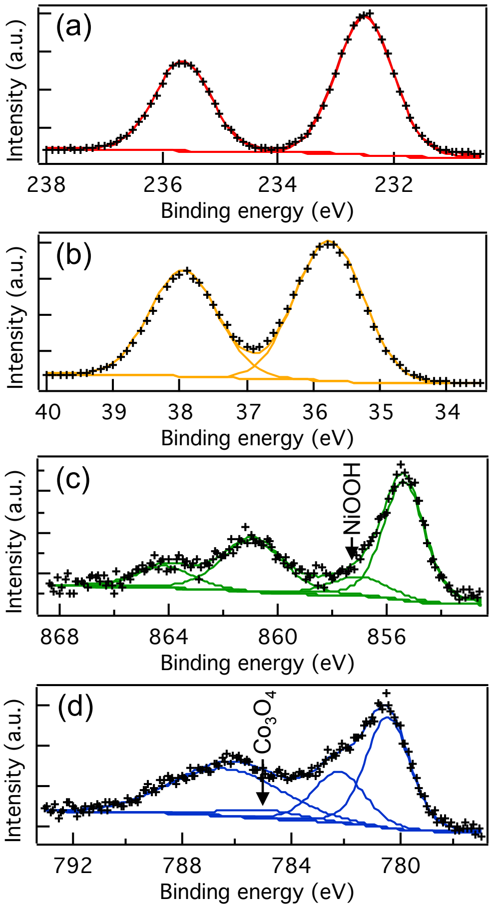

Fig. 7.2. XPS spectra of metal oxide NP films. (a) Mo 3d spectra for MoO_3. (b) W 4f spectra for WO_3. (c) Ni $2p_{3/2}$ spectra for NiO_x. NiOOH peak is labeled, and other peaks correspond to NiO or $Ni(OH)_2$. (d) Co $2p_{3/2}$ spectra for CoO_x. Co_3O_4 peak is labeled, and other peaks correspond to CoO or $Co(OH)_2$. Crosses represent experimental data and lines represent fit to the data.

7.3.2 OPV Performance

We examined the performance of metal oxide NP films as HTLs using conventional PCDTBT:$PC_{71}BM$ OPVs (**Fig. 7.3a**, inset). **Fig. 7.3a** shows that all devices with metal oxide NP HTLs perform similarly to references devices with PEDOT:PSS HTL under AM1.5 100mW/cm^2 illumination. Compared to the device without HTL (**Fig. 7.3a**, purple crosses), the devices with HTL exhibit significantly higher V_{oc} (**Table 7.2**) due to the larger drift field established between the high Φ HTL and Ca. The devices with HTL also exhibit much smaller standard deviations in V_{oc} and power conversion efficiency PCE (**Table 7.2**), highlighting the importance of the HTL in creating a uniform electrical contact between the BHJ and the anode. Examining the data in detail, devices with *n*-type MoO_3 NP (**Fig. 7.3a**, red squares) and WO_3 NP (**Fig. 7.3a**, orange triangles) HTLs exhibit slightly lower short circuit current density J_{sc} compared to reference devices (Figure 3a, black circles), leading to small reductions in PCE (**Table 7.2**). In contrast, devices with *p*-type NiO_x NP (**Fig. 7.3a**, green inverted triangles) and CoO_x NP (**Fig. 7.3a**, blue diamonds) HTLs exhibit similar J_{sc} and PCE as the reference devices. We also compared poly(3-hexylthiophene):phenyl-C_{61}-butyric acid methyl ester (P3HT:$PC_{61}BM$) devices with different HTLs and found that performance identical to reference devices can be achieved using MoO_3, WO_3, and NiO_x NP HTLs. We note that to optimize OPV performance, the thickness of WO_3, NiO_x, and CoO_x NP HTLs must be decreased by diluting the NP suspensions to ¼ of the concentration of the MoO_3 NP suspension.

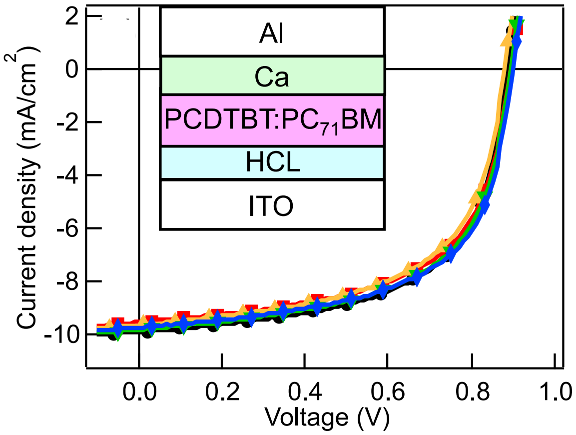

Fig. 7.3. J-V response under AM 1.5 100 mW/cm2 through a 2.5 mm diameter aperture for PCDTBT:PC71BM OPVs with different HTLs. Conventional devices with PEDOT:PSS (black circles), MoO_3 NP (red squares), WO_3 NP (orange triangles), NiO_x NP (green inverted triangles), and CoO_x NP (blue diamonds). Device parameters are given in **Table 7.2**. Inset: conventional device architecture.

This effect can be explained by comparing current density-voltage (J-V) curves of P3HT:PC_{61}BM devices with MoO_3 and NiO_x NP HTLs of different thicknesses. When MoO_3 NP HTL thickness was varied, we found minimal effect on the J-V curves. In contrast, when NiO_x NP HTL thickness was increased, the J-V curve developed a distinct S-shape, significantly decreasing device FF. S-shaped J-V curves have been attributed to inefficient collection of one type of carriers that can be caused by low contact layer conductivity, changes in recombination, or variable electric field distributions, which depends on the specific metal oxide HTL[106]. Thus, by optimizing the thicknesses of metal oxide NP HTLs, performance matching PEDOT:PSS is achieved for conventional

$PCDTBT:PC_{71}BM$ and $P3HT:PC_{61}BM$ OPVs. Decreasing HTL thickness from the optimal values lowered device yield.

Table 7.2. Performance of conventional $PCDTBT:PC_{71}BM$ OPVs with different HTLs under AM1.5 100 mW/cm^2 illumination through a 2.5 mm diameter aperture.

HTL	V_{oc} (V)	J_{sc} (mA/cm^2)	FF	PCE (%)
PEDOT:PSS	0.887 ± 0.005	9.95 ± 0.13	0.604 ± 0.008	5.33 ± 0.13
MoO_3 NP	0.895 ± 0.005	9.57 ± 0.10	0.596 ± 0.005	5.12 ± 0.03
WO_3 NP	0.882 ± 0.004	9.68 ± 0.07	0.587 ± 0.004	5.02 ± 0.04
NiO_x NP	0.895 ± 0.006	9.85 ± 0.11	0.598 ± 0.008	5.27 ± 0.11
CoO_x NP	0.900 ± 0.000	9.77 ± 0.10	0.606 ± 0.006	5.33 ± 0.05

7.4 Conclusions

In conclusion, we demonstrate a general method to synthesize stable suspensions of metal oxide NPs using controlled oxidative dissolution of micron sized metal powders with H_2O_2 in n-butanol. The small NP diameters of 1-2 nm enable solution processing of *n*-type and *p*-type metal oxide NP films on ITO with electronic properties comparable to solution processed and vacuum deposited counterparts, without the need for any post processing. Due to their high Φ values, the metal oxide NP films exhibit excellent performance as HTLs in conventional OPVs, with PCE in most cases identical to the PEDOT:PSS HTL reference. Due to the simplicity and generality of the technique, synthesis of other ultrasmall NPs with tailored properties, e.g. ternary/quaternary and doped metal oxide NPs, should be achievable, with potential applications in many areas, such as photovoltaics, thin film transistors, batteries, and catalysis.

8 Solution Processed Transition Metal Dichalcogenides for Electronic Application

8.1 Introduction

The two-dimensional transition meal dichalcogenides (TMDs) are highly anisotropic layered, graphene-like compounds that are of great interest in basic research due to a large variety of electronic, optical, mechanical and thermal properties that makes them excellent candidates for high-gain photo-detection, among others, because the charge carriers in these materials show large mobility. [107-109]. Furthermore, the extraordinary opaque property of 2D materials in addition to their excellent conductivity makes them highly applicable as electrodes in many electronic devices, such as solar cell[110].

Many 2D materials exist in bulk form as stacks of strongly bonded layers with weak interlayer attraction, allowing exfoliation into individual atomically thin layers[111]. These materials have the formula MX_2, where M is a transition metal element from group IV, V, or VI, and X is a chalcogen (S, Se or Te). They form layered structures of the form X-M-X, with the chalcogen atoms in two hexagonal planes separated by a plane of metal atoms, as shown in **Fig. 8.1**.

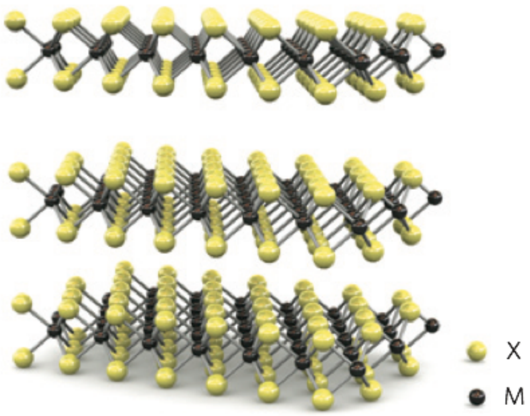

Fig. 8.1. Three dimensional schematic representation of a typical MX_2 structure, with chalcogen atoms (X) in yellow and metal atoms (M) in grey[112].

Flexibility and transparency are also desirable characteristics for next-generation electronics. Researchers are now turning to TMDs as ultrathin materials with tunable bandgaps that can be used in all sort of electronic applications[107]. In some semiconducting TMDs, for example MoS_2, there is a transition from an indirect bandgap (1.3 eV) in the bulk to a direct bandgap in the single-layer form (1.8 eV)[113] as shown in **Fig. 8.2**.

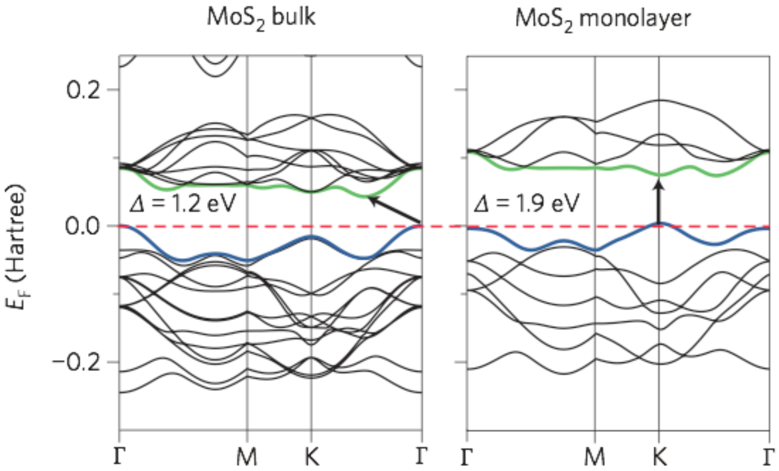

Fig. 8.2. Band structures calculated from first-principles density functional theory (DFT) for bulk and monolayer MoS_2[113].

The presence of bandgap in most semiconducting TMDs, whether in bulk or monolayer, are comparable to the bandgap in silicon making them suitable for use in a wide range of electronic applications. Furthermore, the relatively high Earth abundance of TMDs and their direct bandgaps in the visible range make them attractive as the light-absorbing material in alternative thin-film solar cells[114].

Reliable production of TMDs with uniform properties is essential for translating their electronic and optical properties into applications[107]. Stoichiometry, size, layer thickness, and electronic properties of TMDs may vary depending on the method employed to obtain single or multilayers of TMD nanoflakes: mechanical exfoliation, liquid exfoliation, CVD, epitaxial growth, and solvothermal synthesis have all been used[107,115]. Solution-based colloidal synthetic route for TMDs can be useful because it represents mild reaction conditions and easy tunability in terms of size, composition, and monodispersity[116]. Current reports on solvothermal synthesis of layered TMD nanocrystals in nanometric size are scarce[117].

Although TMDs have been widely studied for decades, their role as near-atomically thin materials is new. Recently a BHJ solar cell made from TiO_2 nanoparticles, MoS_2 atomic layer nanosheets and P3HT was reported with 1.3% photoconversion efficiency[118]. This is a clear example of effective photo-absorption of MoS_2 nanoflakes and the photovoltaic performance shown by the BHJ solar cell suggests that layered semiconductors could be viable material candidates for solar cell applications.

8.2 Electronic Structure Measurements of 2-D Materials

This chapter describes the simplified band structure for a semiconductor material and the characterization techniques used for electronic structure measurements of 2-D materials. In addition, there will be a brief discussion about results obtained from mineral TMDs using these characterization techniques.

A simplified band structure for a semiconductor is shown in **Fig. 8.3**. For semiconductors, the fundamental band gap (E_g) is framed by the valence band maximum (E_{VBM}) and conduction band minimum (E_{CBM}). The work function of a material (F) is the energy required to remove and electron from the Fermi energy to the vacuum level ($E_{VAC} - E_F$). Finally, the ionization energy (IE) is the energy required to remove an electron from the valence band maximum to the vacuum level[119].

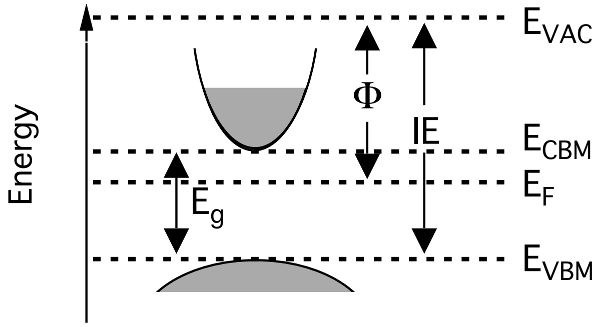

Fig. 8.3. Schematic semiconductor band structure and energy levels.

8.2.1 Kelvin Probe for Work Function Measurements

The work function of a material can be measured using different methods, including ultraviolet photoelectron spectroscopy (UPS) and Kelvin Probe (KP). Owing to the fact that the work function of a material can be extremely sensitive to the surrounding environment, UPS is the most commonly cited method because it occurs under ultra-high vacuum[119].

Unlike UPS, the Kelvin probe does not require ultra-high vacuum conditions to measure work function. Therefore, it offers a distinct advantage over UPS of being able to quickly screen the work function of many samples under ambient conditions. Additionally, the KP also has higher resolution (5–20 meV vs. 100 meV in UPS)[119], which is useful for discerning small changes in sample work function.

The Kelvin probe is a non-contact technique employing a vibrating capacitor to measure the work function difference between a flat probe and the surface of a sample. When brought into close proximity of the surface, the vacuum levels are aligned, but each material (probe and sample) has a different work functions (**Fig. 8.4**, left). By connecting the two materials externally, electrons flow from the lower Φ to the higher Φ so that, equal and opposite surface charges are formed and the Fermi energies are equal. In addition, an electrostatic potential between the tip and sample is generated called the contact potential difference or V_{CPD}, which equals the Φ difference between the tip and the sample (**Fig. 8.4**, center). In this equilibrated state, the potential field equals the work function between the materials. V_{CPD} can be determined by applying a backing potential (V_b) until the field between the two materials is zeroed (**Fig. 8.4**, right)[119]. By knowing the work function of the tip, the work function of the sample can be obtained.

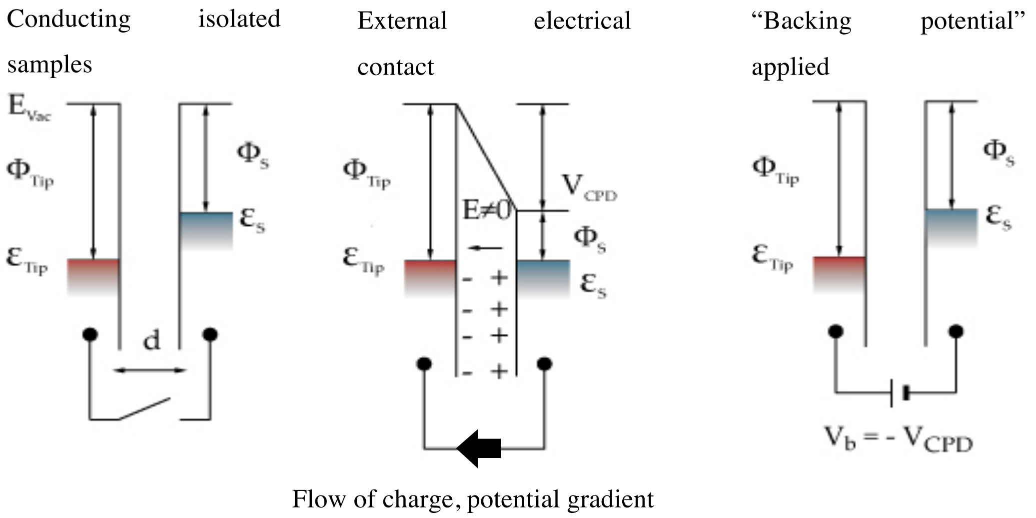

Fig. 8.4. Energy alignment in Kelvin probe measurements in floating (left), short-circuit (center), and voltage-nulling situations (right) [119].

8.2.2 Photoelectron Spectroscopy in Air

The ionization energy (IE) of a material can be measured by photoelectron spectroscopy in air (PESA). This is a non-contact, non-destructive technique that employs an open counter electron detector operated under atmospheric pressure with a low photoexcitation energy UV source (3.4 – 6.2 eV). UV-rays emitted from deuterium lamp are set through a grating monochromator, and then focused on a sample surfaces (spot diameter of 2 mm[120]) in air. The spectra are acquired by increasing the energy of UV photon from 3.4 eV to 6.2 eV, with a 0.05 eV step. When the energy of UV ray is higher than the IE of the sample material, the photoelectrons are emitted from the sample surface and ionize the O_2 in the air. These ions are detected and counted in the air by the open counter. The crossing point of the background and the yield line is called photoemission threshold energy. If the sample is a metal, the relationship between the photon energy and the square root of yield looks linear, the photoemission threshold energy indicates the work function of the metal. If the sample is semiconductor, the cube root of yield shows a linear relationship with the incident photon energy, and the photoemission threshold energy equals the IE of the semiconductor[121].

8.3 Experimental

Motivated by these attractive properties of TMD and encouraging electronic applications, we explored the synthesis of colloidal MoS_2 nanoflakes. Following a microwave-assisted synthesis procedure modified from Joo and colleagues[122]. We selected this approach because it has been shown to yield various semiconducting metal sulfide nanocrystals employing thermolysis of organometallic precursors with low size polydispersity and good stability.

MoS_2 nanoflakes were synthesized from the reaction of molybdenum(V) chloride and sulfur powder in oleylamine in the presence of 1,2-hexadecanediol. For the microwave synthesis, $MoCl_5$ (0.05 M) (Aldrich) with 1,2-hexadecanediol (0.05 M) (Alfa Aesar) were dissolved in oleylamine (technical grade 70%, Aldrich), added to a previous dissolved solution of sulfur (Alfa Aesar) in oleylamine (0.6 M). The solution was placed in a microwave reactor (CEM Discovery) containing a single-mode 2.54 GHz microwave cavity. The solution were maintained at 100 °C for 1 hour to completely dissolve the precursors, and reacted at different temperatures ranging from 140°C to 220 °C for 15 minutes and 1 hour, resulting in black colloidal solution (**Fig. 8.5**).

Fig. 8.5. Schematic of microwave synthesis of MoS_2 nanoflakes.

Anhydrous ethanol was added in order to cause the MoS_2 nanoflakes to be precipitated. The precipitate was retrieved by centrifugation and washed four more times using anhydrous ethanol to completely eliminate any organic residual. The nanoflakes were then dispersed in dichloromethane (DCM).

To determine the nanoflake size and distribution, an aliquot of the resulting suspension was diluted by a factor of 100 with DCM, agitated in an ultrasonic bath for 5 min and analyzed by dynamic light Scattering (DLS) under backscattering conditions using a Malvern Zetasizer. For TEM, MoS_2 suspension was diluted 5 times with DCM, drop casted on a TEM grid (01824, Ted Pella), and imaged at 200 kV with a JEOL JEM2100. For Φ and XPS measurements, MoS_2 suspension was dropcasted on p-type Si(100) substrates (10-20 Wcm, University Wafers) that had been cleaned by rinsing with IPA and H_2O, follow by UV-O_3 cleaning for 20 min. For PESA measurements MoS_2 films were drop casted on glass slides previously cleaned with the same procedure as Si substrates. Φ was measured in air using a scanning Kelvin probe (SKP 5050, KP Technology) with Au as the reference material (Φ = 5.15 eV). XPS was measured using a Ulvac-PHI VersaProbe 2 with monochromated Al Kα source (1486.8 eV). All spectra were collected at an angle of 45° to the sample surface with energy step of 0.1 eV and pass energy of 23.5 eV, and were fitted using commercial software (MultiPak, Ulvac-PHI). PESA was performed using a RKI Instruments Model AC-2 system with 100 nW deuterium lamp power with a step of 0.05 eV. Topography measurement was performed using an Asylum Research MFP-3D atomic force microscope

(AFM).

8.4 Results and discussion

We found that microwave heating of precursor solution resulted in a black suspension of MoS_2 (**Fig. 8.5**). The suspension showed excellent stability and remained dispersed for more than 30 days. DLS of the synthesized MoS_2 nanoflakes shows that the MoS_2 nanoflakes size depends strongly on the reaction temperature and time. 15 min reaction at 220°C produces 142 ± 23 nm lateral size (**Fig. 8.6c**). SAED pattern from MoS_2 nanoflake surface depicts hexagonal lattice structure, consistent with 2H phase (**Fig. 8.6d**).

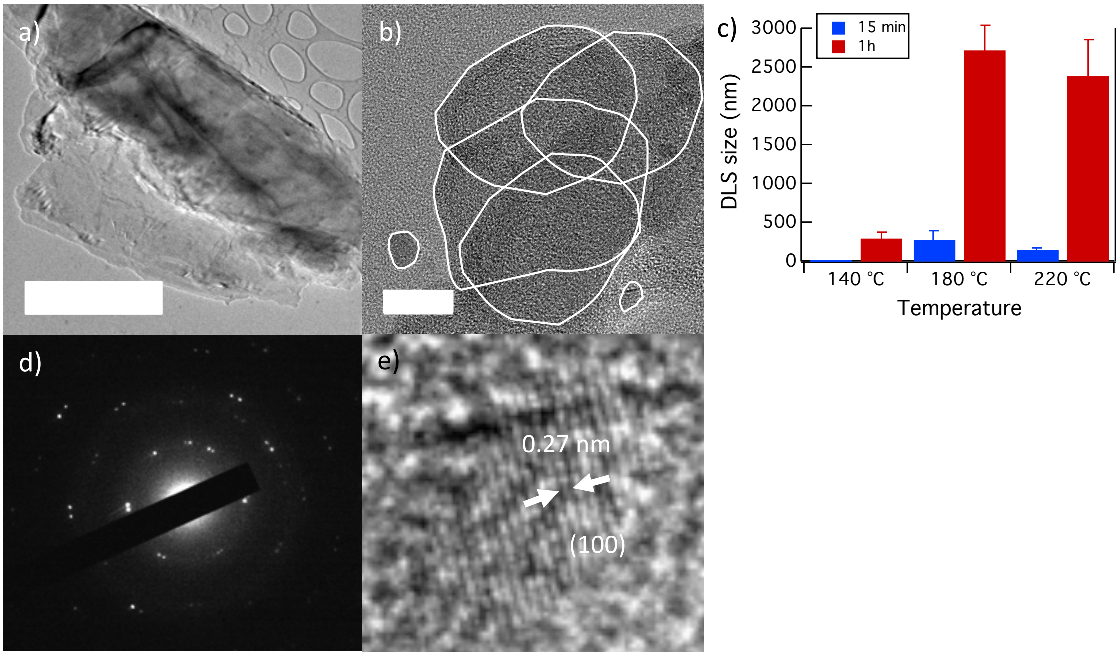

Fig. 8.6. TEM characterization of MoS_2 nanoflakes. (a) TEM image, scale bar 2 μm. (b) A typical HRTEM image of MoS_2 nanoflakes,

scale bar 20 nm. (c) DLS size distribution histogram. (d) The SAED pattern from the MoS_2 surface shown in (a). (e) Enlarged HRTEM image of MoS_2 nanoflake, the measured d spacing distance is around 0.27 nm

The stoichiometry of MoS_2 nanoflakes was characterized by x-ray photoelectron spectroscopy (XPS). The Mo3d, S2s, and S2p spectra of MoS_2 nanoflakes synthesized at different conditions on silicon (crosses) and curve fit (solid) (**Fig. 8.7a,b**), are consistent with 2H phase of MoS_2[123]. Raman spectra of MoS_2 nanoflakes is can be seen in **Fig. 8.7c**, showing in plane E^1_{2g} and out of plane A_{1g} peaks, consistent with 2H phase[124].

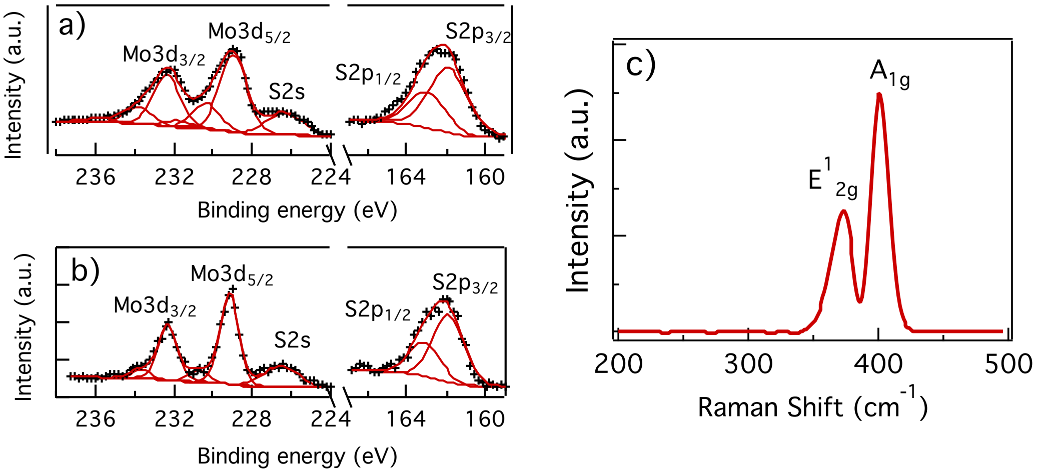

Fig. 8.7. XPS spectra showing Mo 3d, S 2s, and S2p core level peak regions for samples synthesized at (a) 180 °C -15 min, (b) 200 °C -15 min. (c) Raman spectra of MoS_2 nanoflake synthesized at 220 °C-15 min.

An AFM topographic image of a MoS_2 nanoflake is shown in **Fig. 8.8** (left). Cross-sectional plot along the red line from AFM image of a 6.4

Å thick single layer MoS$_2$ nanoflake synthesized at 140 °C - 1h (**Fig. 8.8**, right), matching (002) interplanar distance, indicating a single layer flake.

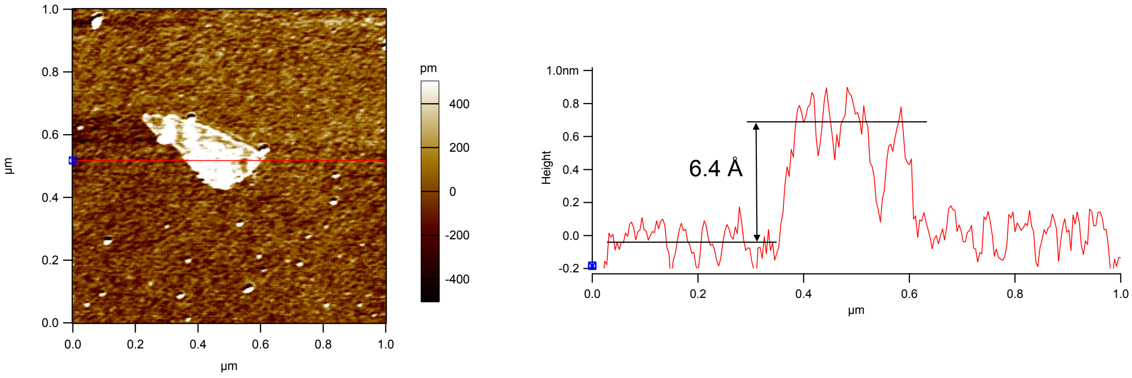

Fig. 8.8. Atomic force microscopy image of a single layer MoS$_2$ nanoflake (left). Cross-sectional plot along the red line in left (right).

IE of MoS$_2$ nanoflakes were measured by photoelectron spectroscopy in air (PESA) (**Fig. 8.9a**) yielding values of 4.85 eV. The synthesis temperature and time do not have effect on IE, as shown in **Fig. 8.9b**. The Φ of the MoS$_2$ nanoflakes was measured using scanning Kelvin probe, and was found to be 4.50 ± 0.04 eV the highest value, when synthesized at 180 °C-15 min (**Fig. 8.9b**). Assuming a bandgap of 1.3 eV[125], these MoS$_2$ nanoflakes show a p-type behavior (**Fig. 8.9c**).

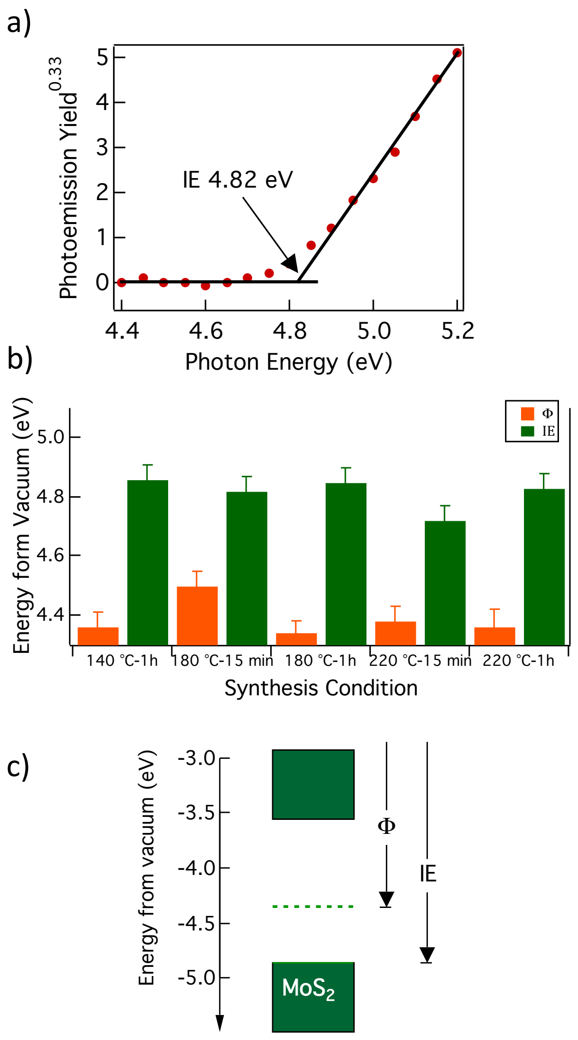

Fig. 8.9. (a) PESA spectrum of MoS_2 nanoflakes synthesized at 180 °C -15 min. (b) Φ and IE histogram for MoS_2 synthesized at different conditions. (c) Band diagram of MoS_2 synthesized at 180 °C –15 min, constructed from IE and F measurements, using a reference bandgap value of 1.3 eV[125].

8.5 Conclusions

We have demonstrated the ability to synthesize MoS_2 nanoflakes by solvothermal method by microwave heating. Results confirmed by XPS and Raman spectroscopy the presence of MoS_2 2H phase. In addition, SAED and TEM confirmed MoS_2 hexagonal structure. MoS_2 nanoflake thickness is consistent with a single-layer flake. Finally, according to PESA and Kelvin probe measurements, IE of MoS_2 nanoflakes remained unaffected by synthesis conditions, whereas Φ presents a maximum when MoS_2 is synthesized at 180 °C for 15 minutes.

9 General Conclusions

In summary, we have demonstrated the influence of the underlying layer on the BHJ layer morphology. We showed that phase segregation leads to a reduction of interfacial area and lower PCBM concentrations outside of the clusters in the active layer, resulting in drastic reduction of OPV parameters due to both low charge generation and high bimolecular recombination. We found a simple solution by rinsing the pyrolyzed MEA-containing ZnO films with MOE or using a ZnO recipe without MEA significantly reduced the formation of PCBM clusters and produced devices with good performance.

We demonstrated that *in situ* chemical oxidation of MoO_x nanoparticle suspensions with H_2O_2 is a simple but versatile method to control their stoichiometry and electronic properties. Our synthesis resulted in ≤ 1 nm MoO_x nanoparticles with high work function and almost entirely MoO_3, properties which are desirable for HTL material in OPV devices. We established a clear correlation between the work function and the Mo^{6+} fraction of the MoO_x, and achieved a continuous tuning of work function. Moreover, the simplicity of the chemical oxidation procedure should be generally applicable in synthesizing other transition oxide nanomaterials with tunable stoichiometry and properties.

Following the MoO_x nanoparticle synthesis, we demonstrate a general method to synthesize stable suspensions of other metal oxide nanoparticles using controlled oxidative dissolution of micron sized metal powders with H_2O_2 in n-butanol. We achieved the deposit of small nanoparticles with diameters of 1-2 nm *n*-type MoO_3 and WO_3, and *p*-type NiO_x and CoO_x films on ITO with electronic properties comparable to solution processed and vacuum deposited counterparts, without the need for any post processing. The metal oxide nanoparticle films exhibit excellent performance as HTLs in OPVs.

Finally, we have demonstrated the ability to synthesize MoS_2 nanoflakes by solvothermal method using microwave heating. Spectroscopy techniques showed the presence of MoS_2 2H phase and SAED and TEM confirmed the hexagonal structure. MoS_2 nanoflake thickness is consistent with a single-layer flake. Finally, according to PESA and Kelvin probe measurements, IE of MoS_2 nanoflakes remained unaffected by synthesis conditions, whereas Φ presents a maximum when MoS_2 is synthesized at 180 °C for 15 minutes. The synthesis of layered graphene-like materials, with electronic, optical, mechanical and thermal properties contributes to the pursuit of materials suitable for flexible electronic applications.

Taken together, the investigations carried out in this thesis contribute positively towards finding routes for low-temperature solution processing of metal-oxides and transition metal dichalcogenides, suitable to replace their vacuum processed analogues and building blocks in large-scale OPVs fabrication.

Future Work

We propose the optimization of the synthesis of MoS_2 nanoflakes. The challenge to develop simple methods for the preparation of high-quallity 2D nanoflakes that are solution-processable at low temperature remains. Exploration of this synthesis method using CS_2 as chalcogen precursor agents in order to get similar Φ and IE to those measured from mineral TMDs [115]. Recently, Jeong *et al.* reported the generation of highly reactive radicals from elemental sulfur during the reaction, which promoted degradation of the structural integrity of 2-D layered nanocrystals[116]. To avoid reactive radical formation, CS_2 was chosen as alternative chalcogen precursor because no radical species are formed when CS_2 is heated in oleylamine[115,116]. In addition to the synthesis, it is necessary to achieve the deposition of functional thin films from these colloidal solutions for applications in energy conversion and flexible electronics. Most methods for the fabrication of thin films of TMDs require high vacuum or high temperature, very few methods have been reported regarding solution-based deposition.

The electronic structure of these nanoflakes should be studied with Kelvin probe and PESA measurements. In addition, size and crystallinity will be examined by TEM, and stoichiometry characterization of these semiconductor 2D materials will be performed by XPS studies. For the second part of this work, we propose the synthesis of other TMDs (MoSe2, WS_2, WSe_2) following this solvothermal method, the fabrication of electronic devices using films casted from solution processed TMDs, such as solar cells.

Recently, it was reported that films prepared from exfoliated WS_2 and MoS_2 solutions show high smoothness compared to bare ITO, leading to an improvement of the OPV when these materials are used as interfacial layer[126].

Achievements

Publications:

1. Y.-J. Lee, **D. Barrera**, K. Luo, J.W.P. Hsu, In Situ Chemical Oxidation of Ultrasmall MoO$_x$ Nanoparticles in Suspensions, Nanotechnology 195761 (2012). doi:10.1155/2012/195761.

2. **D. Barrera**, Y.-J. Lee, J.W.P. Hsu, Influence of ZnO sol-gel electron transport layer processing on BHJ active layer morphology and OPV performance, Sol. Energ. Mat. Sol. Cells. 125 (2014) 27–32. doi:10.1016/j.solmat.2014.02.014.

3. Y.-J. Lee, J. Wang, J.W. Hsu, **D. Barrera**, General method to synthesize ultrasmall metal oxide nanoparticle suspensions for hole contact layers in organic photovoltaic devices, MRS Commun. 5 (2015) 45-50. doi:10.1557/mrc.2015.5.

4. P. Huang, J. Du, S. S. Gunathilake, E. A. Rainbolt, J. W. Murphy, K. T. Black, **D. Barrera**, J.W.P. Hsu, B. E. Gnade, M. C. Stephan, M. C. Biewer, Benzodifuran and benzodithiphene donor-acceptor polymers for bulk heterojunction solar cells, J. Mater. Chem. A. 3 (2015) 6980. doi:10.1039/c5ta00936g

5. J. Wang, V. Ibarra, **D. Barrera**, L. Xu, Y.-J. Lee, J.W.P. Hsu, Solution Synthesized p-Type Copper Gallium Oxide Nanoplates as Hole Transport Layer for Organic Photovoltaic Devices, J. Phys. Chem. Lett. 6 (2015) 1071–1075. doi:10.1021/acs.jpclett.5b00236.

6. R. Addou, S. McDonnell, **D. Barrera**, Z. Guo, A. Azcatl, J. Wang, H. Zhu, C. L. Hinkle, M. Quevedo-Lopez, H. N Alshareef, L. Colombo, J. W. P. Hsu, and R. M. Wallace, Conductivity Variation of Exfoliated Natural MoS_2 Crystals, **in rev.** ACS Nano (2015).

7. S. KC, R. Addou, **D. Barrera**, R. C. Longo, J.W.P. Hsu, R. M. Wallace, and K. J. Cho, Understanding the Unprecedented Mechanism of Air Stability of Two-Dimensional layered Transition Metal Dichalcogenide Surfaces, **in prep**.

Presentations:

- Y.-J. Lee, **D. Barrera**, J. Wang, G. Gao, S. Cheng, J.W.P. Hsu, Low Temperature Solution Processing of Inorganic Nanoparticles for Contact Layers in Organic Photovoltaics, Electronic Materials and Applications, Orlando, FL, January 2013, oral presentation.
- Y.-J. Lee, J. Wang, **D. Barrera**, G. Gao, J.W.P. Hsu, Low Temperature Solution Processing of Inorganic Nanoparticles for Contact Layers in Organic Photovoltaics, Forum on New Materials, Montecatini Terme, Italy, June 2014, oral presentation.
- Y.-J. Lee, **D. Barrera**, J. Wang, J.W.P. Hsu, General Method to Synthesize Ultrasmall Metal Oxide Nanoparticle Suspensions as Hole Contact Layers in Organic Photovoltaic Devices, 2014 Fall Materials Research Society Meeting, Boston, MA, December 2015, poster.
- **D. Barrera**, Y. Lee, J. Wang, L. Cheng, J. Kim, J. W. P. Hsu, Synthesis, Characterization, and Electronic Structure of Solution Processed Ultrathin MoS_2, 2015 Spring Materials Research Society Meeting, San Francisco, CA, April 2015, poster.

- R. Addou, H. Zhu, **D. Barrera**, Santosh KC., J. Wang, K. Cho, J. Hsu, R. M. Wallace, Reactivity of Transition Metal Dichalcogenide, 2015 Spring Materials Research Society Meeting, San Francisco, CA, April 2015, oral presentation.

References

1. N. Grossiord, J. M. Kroon, R. Andriessen, and P. W. Blom, *Organic Electronics*, 2012, **13**, 432–456.
2. J. Ahmad, K. Bazaka, L. J. Anderson, R. D. White, and M. V. Jacob, *Renew. Sustainable Energy Rev.*, 2013, **27**, 104–117.
3. C. J. Brabec, *Sol. Energ. Mat. Sol. Cells*, 2004, **83**, 273–292.
4. S. E. Shaheen, D. S. Ginley, and G. E. Jabbour, *MRS Bull.*, 2005, **30**, 10–19.
5. L. El Chaar, L. A. Iamont, and N. El Zein, *Renew. Sustainable Energy Rev.*, 2011, **15**, 2165–2175.
6. B. Kippelen and J.-L. Brédas, *Energy Environ. Sci.*, 2009, **2**, 241–332.
7. K. Zilberberg, J. Meyer, and T. Riedl, *J. Mater. Chem. C*, 2013, **1**, 4796.
8. M. Hösel, R. R. Søndergaard, M. Jørgensen, and F. C. Krebs, *Energy Technology*, 2013, **1**, 102–107.
9. Y.-J. Lee, J. Wang, S. R. Cheng, and J. W. P. Hsu, *ACS Appl. Mater. Interfaces*, 2013, **5**, 9128–9133.
10. J. Gilot, M. M. Wienk, and R. A. J. Janssen, *Appl. Phys. Lett.*, 2007, **90**, 143512–143512–3.
11. S. K. Hau, H.-L. Yip, N. S. Baek, J. Zou, K. O'Malley, and A. K. Y. Jen, *Appl. Phys. Lett.*, 2008, **92**, 253301.
12. N. Li, T. Stubhan, N. A. Luechinger, S. C. Halim, G. J. Matt, T. Ameri, and C. J. Brabec, *Organic Electronics*, 2012.
13. S. R. Hammond, J. Meyer, N. E. Widjonarko, P. F. Ndione, A. K. Sigdel, A. Garcia, A. Miedaner, M. T. Lloyd, A. Kahn, and D. S. Ginley, *J. Mater. Chem.*, 2012, **22**, 3249–3254.
14. K. Zilberberg, S. Trost, H. Schmidt, and T. Riedl, *Adv. Energy Mater.*, 2011, **1**, 377–381.
15. J. You, L. Dou, K. Yoshimura, T. Kato, K. Ohya, T. Moriarty, K. Emery, C.-C. Chen, J. Gao, and G. Li, *Nat. Commun.*, 2013, **4**, 1446.
16. R. Steim, F. R. Kogler, and C. J. Brabec, *J. Mater. Chem.*, 2010, **20**, 2499–2512.
17. P. W. Blom, V. D. Mihailetchi, L. J. A. Koster, and D. E. Markov, *Adv. Mater.*, 2007, **19**, 1551–1566.
18. X. Yang, J. Loos, S. C. Veenstra, W. J. H. Verhees, M. M.

Wienk, J. M. Kroon, M. A. J. Michels, and R. A. J. Janssen, *Nano Lett.*, 2005, **5**, 579–583.
19. S. S. V. Bavel, E. Sourty, G. de With, and J. Loos, *Nano Lett.*, 2009, **9**, 507–513.
20. P. V. Kamat, *J. Phys. Chem. C*, 2007, **111**, 2834–2860.
21. C. D. Dimitrakopoulos and D. J. Mascaro, *IBM J. Res. Dev.*, 2001, **45**, 11–27.
22. H. Hoppe and N. S. Sariciftci, *J. Mater. Res.*, 2004, **19**, 1924–1945.
23. F. Liu, S. Shao, X. Guo, Y. Zhao, and Z. Xie, *Sol. Energ. Mat. Sol. Cells*, 2010, **94**, 842–845.
24. M. Ghasemi Varnamkhasti, H. R. Fallah, M. Mostajaboddavati, R. Ghasemi, and A. Hassanzadeh, *Sol. Energ. Mat. Sol. Cells*, 2012, **98**, 379–384.
25. Y. Zang, J. Huang, H. Li, J. Yu, and Y. Jiang, *Energy Procedia*, 2011, **12**, 513–518.
26. Y.-J. Lee, J. Yi, G. F. Gao, H. Koerner, K. Park, J. Wang, K. Luo, R. A. Vaia, and J. W. P. Hsu, *Adv. Energy Mater.*, 2012, **2**, 1193–1197.
27. V. Shrotriya, G. Li, Y. Yao, C.-W. Chu, and Y. Yang, *Appl. Phys. Lett.*, 2006, **88**, 073508–073508–3.
28. K. Zilberberg, S. Trost, J. Meyer, A. Kahn, A. Behrendt, D. Lützenkirchen-Hecht, R. Frahm, and T. Riedl, *Adv. Funct. Mater.*, 2011, **21**, 4776–4783.
29. E. L. Ratcliff, J. Meyer, K. X. Steirer, N. R. Armstrong, D. Olson, and A. Kahn, *Organic Electronics*, 2012, **13**, 744–749.
30. T. Salim, Z. Yin, S. Sun, X. Huang, H. Zhang, and Y. M. Lam, *ACS Appl. Mater. Interfaces*, 2011, **3**, 1063–1067.
31. M. S. White, D. C. Olson, S. E. Shaheen, N. Kopidakis, and D. S. Ginley, *Appl. Phys. Lett.*, 2006, **89**, 143517.
32. J. Y. Kim, K. Lee, N. E. Coates, D. Moses, T.-Q. Nguyen, M. Dante, and A. J. Heeger, *Science*, 2007, **317**, 222–225.
33. X. Chen, C. Zhao, L. Rothberg, and M.-K. Ng, *Appl. Phys. Lett.*, 2008, **93**, 123302.
34. G. Zhao, Y. He, and Y. Li, *Adv. Mater.*, 2010, **22**, 4355–4358.
35. M. O. Reese, M. S. White, G. Rumbles, D. S. Ginley, and S. E. Shaheen, *Appl. Phys. Lett.*, 2008, **92**, 053307.
36. H. Spanggaard and F. C. Krebs, *Sol. Energ. Mat. Sol. Cells*, 2004, **83**, 125–146.
37. S. O. Kasap, *Principles of Electronic Materials and Devices*, McGraw-Hill, New York, 3rd edn. 2007, vol. 81.
38. S. R. Cowan, J. Wang, J. Yi, Y.-J. Lee, D. C. Olson, and J. W.

P. Hsu, *J. Appl. Phys.*, 2013, **113**, 154504.

39. L. Bahadur, M. Hamdani, J. F. Koenig, and P. Chartier, *Sol. Energ. Mater.*, 1986, **14**, 107–120.
40. L. Znaidi, G. Soler Illia, S. Benyahia, C. Sanchez, and A. V. Kanaev, *Thin Solid Films*, 2003, **428**, 257–262.
41. X. L. Cheng, H. Zhao, L. H. Huo, S. Gao, and J. G. Zhao, *Sensor. Actuat. B-Chem.*, 2004, **102**, 248–252.
42. H. Li, J. Wang, H. Liu, H. Zhang, and X. Li, *J. Cryst. Growth*, 2005, **275**, 943–946.
43. Y. Ohya, H. Saiki, and Y. Takahashi, *J. Mater. Sci.*, 1994, **29**, 4099–4103.
44. M. Ohyama, H. Kouzuka, and T. Yoko, *Thin Solid Films*, 1997, **306**, 78–85.
45. H. T. Nguyen, N. D. Nguyen, and S. Lee, *Nanotechnology*, 2013, **24**, 115201.
46. J. S. Park, J. M. Lee, S. K. Hwang, S. H. Lee, H.-J. Lee, B. R. Lee, H. I. Park, J.-S. Kim, S. Yoo, and M. H. Song, *J. Mater. Chem.*, 2012, **22**, 12695–12700.
47. T. Kuwabara, Y. Kawahara, T. Yamaguchi, and K. Takahashi, *ACS Appl. Mater. Interfaces*, 2009, **1**, 2107–2110.
48. Y. Sun, J. H. Seo, C. J. Takacs, J. Seifter, and A. J. Heeger, *Adv. Mater.*, 2011, **23**, 1679–1683.
49. C. E. Small, S. Chen, J. Subbiah, C. M. Amb, S.-W. Tsang, T.-H. Lai, J. R. Reynolds, and F. So, *Nature Photon.*, 2011, **6**, 115–120.
50. A. K. K. Kyaw, X. W. Sun, C. Y. Jiang, G. Q. Lo, D. W. Zhao, and D. L. Kwong, *Appl. Phys. Lett.*, 2008, **93**, 221107.
51. C. M. Amb, M. R. Craig, U. Koldemir, J. Subbiah, K. R. Choudhury, S. A. Gevorgyan, M. Jørgensen, F. C. Krebs, F. So, and J. R. Reynolds, *ACS Appl. Mater. Interfaces*, 2012, **4**, 1847–1853.
52. M. Lira-Cantu and F. C. Krebs, *Sol. Energ. Mat. Sol. Cells*, 2006, **90**, 2076–2086.
53. M. T. Lloyd, C. H. Peters, A. Garcia, I. V. Kauvar, J. J. Berry, M. O. Reese, M. D. McGehee, D. S. Ginley, and D. C. Olson, *Sol. Energ. Mat. Sol. Cells*, 2011, **95**, 1382–1388.
54. S. B. Jo, J. H. Lee, M. Sim, M. Kim, J. H. Park, Y. S. Choi, Y. Kim, S.-G. Ihn, and K. Cho, *Adv. Energy Mater.*, 2011, **1**, 690–698.
55. K. C. Choi, E. J. Lee, Y. K. Baek, M. J. Kim, Y. D. Kim, and P. W. Shin, *R. Soc. Chem. Adv.*, 2014, **4**.
56. W. Ma, C. Yang, X. Gong, K. Lee, and A. J. Heeger, *Adv.*

Funct. Mater., 2005, **15**, 1617–1622.
57. S. van Bavel, E. Sourty, G. de With, S. Veenstra, and J. Loos, *J. Mater. Chem.*, 2009, **19**, 5388–5393.
58. R. A. Marsh, J. M. Hodgkiss, S. Albert-Seifried, and R. H. Friend, *Nano Lett.*, 2010, **10**, 923–930.
59. O. Oklobia and T. S. Shafai, *Sol. Energ. Mat. Sol. Cells*, 2013, **117**, 1–8.
60. T. J. Savenije, J. E. Kroeze, X. Yang, and J. Loos, *Adv. Funct. Mater.*, 2005, **15**, 1260–1266.
61. S. S. van Bavel, M. Bärenklau, G. de With, H. Hoppe, and J. Loos, *Adv. Funct. Mater.*, 2010, **20**, 1458–1463.
62. D. Chirvase, J. Parisi, J. C. Hummelen, and V. Dyakonov, *Nanotechnology*, 2004, **15**, 1317.
63. S. Bertho, G. Janssen, T. J. Cleij, B. Conings, W. Moons, A. Gadisa, J. D'Haen, E. Goovaerts, L. Lutsen, and J. Manca, *Sol. Energ. Mat. Sol. Cells*, 2008, **92**, 753–760.
64. B. Watts, W. J. Belcher, L. Thomsen, H. Ade, and P. C. Dastoor, *Macromolecules*, 2009, **42**, 8392–8397.
65. Z. Li, H. C. Wong, Z. Huang, H. Zhong, and C. H. Tan, *Nat. Commun.*, 2013, **4**, 2227.
66. Y.-J. Lee, R. J. Davis, M. T. Lloyd, P. P. Provencio, R. P. Prasankumar, and J. W. P. Hsu, *IEEE J. Sel. Top. Quant. Electron.*, 2010, **16**, 1587–1594.
67. C. Waldauf, M. Morana, P. Denk, P. Schilinsky, K. Coakley, S. A. Choulis, and C. J. Brabec, *Appl. Phys. Lett.*, 2006, **89**, 233517.
68. M. O. Reese, A. K. Sigdel, J. J. Berry, D. S. Ginley, and S. E. Shaheen, *Sol. Energ. Mat. Sol. Cells*, 2010, **94**, 1254–1258.
69. M. N. Kamalasanan and S. Chandra, *Thin Solid Films*, 1996, **288**, 112–115.
70. S. Bandyopadhyay, G. K. Paul, R. Roy, S. K. Sen, and S. Sen, *Mater. Chem. Phys.*, 2002, **74**, 83–91.
71. S. Fujihara, C. Sasaki, and T. Kimura, *Appl. Surf. Sci.*, 2001, **180**, 341–350.
72. H. Bach and D. Krause, *Thin Films on Glass*, Springer, Berlin, 1st edn. 1997.
73. A. S. Aricò, P. Bruce, B. Scrosati, J.-M. Tarascon, and W. van Schalkwijk, *Nat. Mater.*, 2005, **4**, 366–377.
74. D. R. Rolison, *Science*, 2003, **299**, 1698–1701.
75. M. Fernández-García, A. Martínez-Arias, J. C. Hanson, and J. A. Rodriguez, *Chem. Rev.*, 2004, **104**, 4063–4104.
76. M. E. Franke, T. J. Koplin, and U. Simon, *Small*, 2006, **2**, 36–50.
77. A. K. Gupta and M. Gupta, *Biomaterials*, 2005, **26**, 3995–

4021.
78. D. Y. Kim, J. Subbiah, G. Sarasqueta, F. So, H. Ding, and Y. Gao, *Appl. Phys. Lett.*, 2009, **95**, 093304–093304–3.
79. M. Kröger, S. Hamwi, J. Meyer, T. Riedl, W. Kowalsky, and A. Kahn, *Appl. Phys. Lett.*, 2009, **95**, 123301.
80. J. Meyer, R. Khalandovsky, P. Görrn, and A. Kahn, *Adv. Mater.*, 2011, **23**, 70–73.
81. C. Girotto, E. Voroshazi, D. Cheyns, P. Heremans, and B. P. Rand, *ACS Appl. Mater. Interfaces*, 2011, **3**, 3244–3247.
82. M. Jørgensen, K. Norrman, and F. C. Krebs, *Sol. Energ. Mat. Sol. Cells*, 2008, **92**, 686–714.
83. M. T. Lloyd, D. C. Olson, P. Lu, E. Fang, D. L. Moore, M. S. White, M. O. Reese, D. S. Ginley, and J. W. P. Hsu, *J. Mater. Chem.*, 2009, **19**, 7638–7642.
84. I. Bilecka, I. Djerdj, and M. Niederberger, *Chem. Commun.*, 2008, 886.
85. J. G. Choi and L. T. Thompson, *Appl. Surf. Sci.*, 1996, **93**, 143–149.
86. T. C. Arnoldussen, *J. Electrochem. Soc.*, 1976, **123**, 527–531.
87. M. T. Greiner and Z.-H. Lu, *NPG Asia Materials*, 2013, **5**, e55.
88. N. Li, D. Baran, K. Forberich, F. Machui, T. Ameri, M. Turbiez, M. Carrasco-Orozco, M. Drees, A. Facchetti, F. C. Krebs, and C. J. Brabec, *Energy Environ. Sci.*, 2013, **6**, 3407–3413.
89. R. R. Søndergaard, M. Hösel, and F. C. Krebs, *J. Polym. Sci. Part B Polym. Phys.*, 2013, **51**, 16–34.
90. H.-L. Yip and A. K. Y. Jen, *Energy Environ. Sci.*, 2012, **5**, 5994.
91. K. X. Steirer, P. F. Ndione, N. E. Widjonarko, M. T. Lloyd, J. Meyer, E. L. Ratcliff, A. Kahn, N. R. Armstrong, C. J. Curtis, D. S. Ginley, J. J. Berry, and D. C. Olson, *Adv. Energy Mater.*, 2011, **1**, 813–820.
92. C. P. Chen, Y. D. Chen, and S. C. Chuang, *Adv. Mater.*, 2011, **23**, 3859–3863.
93. K. Zilberberg, H. Gharbi, A. Behrendt, S. Trost, and T. Riedl, *ACS Appl. Mater. Interfaces*, 2012, **4**, 1164–1168.
94. F. Xie, W. C. H. Choy, C. Wang, X. Li, S. Zhang, and J. Hou, *Adv. Mater.*, 2013, **25**, 2051–2055.
95. K. X. Steirer, J. P. Chesin, N. E. Widjonarko, J. J. Berry, A. Miedaner, D. S. Ginley, and D. C. Olson, *Organic Electronics*, 2010, **11**, 1414–1418.
96. T. Stubhan, T. Ameri, M. Salinas, J. Krantz, F. Machui, M. Halik, and C. J. Brabec, *Appl. Phys. Lett.*, 2011, **98**, 253308.
97. T. Stubhan, N. Li, N. A. Luechinger, S. C. Halim, G. J. Matt,

and C. J. Brabec, *Adv. Energy Mater.*, 2012, **2**, 1433–1438.
98. T. Yang, M. Wang, Y. Cao, F. Huang, L. Huang, J. Peng, X. Gong, S. Z. D. Cheng, and Y. Cao, *Adv. Energy Mater.*, 2012, **2**, 523–527.
99. J. H. Huang, T. Y. Huang, H. Y. Wei, K. C. Ho, and C. W. Chu, *R. Soc. Chem. Adv.*, 2012, **2**, 7487–7491.
100. E. Redel, C. Huai, Ö. Dag, S. Petrov, P. G. O'Brien, M. G. Helander, J. Mlynarski, and G. A. Ozin, *Small*, 2012, **8**, 3806–3809.
101. S. H. Park, A. Roy, S. Beaupré, S. Cho, N. Coates, J. S. Moon, D. Moses, M. Leclerc, K. Lee, and A. J. Heeger, *Nature Photon.*, 2009, **3**, 297–302.
102. J. Meyer, A. Shu, M. Kröger, and A. Kahn, *Appl. Phys. Lett.*, 2010, **96**, 133308–133308.
103. M. T. Greiner, L. Chai, M. G. Helander, W.-M. Tang, and Z.-H. Lu, *Adv. Funct. Mater.*, 2012, **22**, 4557–4568.
104. M. C. Biesinger, B. P. Payne, A. P. Grosvenor, L. W. Lau, A. R. Gerson, and R. S. C. Smart, *Appl. Surf. Sci.*, 2011, **257**, 2717–2730.
105. E. L. Ratcliff, J. Meyer, K. X. Steirer, A. Garcia, J. J. Berry, D. S. Ginley, D. C. Olson, A. Kahn, and N. R. Armstrong, *Chem. Mater.*, 2011, **23**, 4988–5000.
106. A. Wagenpfahl, D. Rauh, M. Binder, C. Deibel, and V. Dyakonov, *Phys. Rev. B*, 2010, **82**, 115306.
107. Q. H. Wang, K. Kalantar-Zadeh, A. Kis, J. N. Coleman, and M. S. Strano, *Nat. Nanotechnol.*, 2012, **7**, 699–712.
108. W. S. Yun, S. W. Han, S. C. Hong, I. G. Kim, and J. D. Lee, *Phys. Rev. B*, 2012, **85**, 033305.
109. B. Radisavljevic, M. B. Whitwick, and A. Kis, *ACS Nano*, 2011, **5**, 9934–9938.
110. X. Wang, L. Zhi, and K. Müllen, *Nano Lett.*, 2008, **8**, 323–327.
111. K. S. Novoselov, D. Jiang, F. Schedin, T. J. Booth, V. V. Khotkevich, S. V. Morozov, and A. K. Geim, *Proc. Natl. Acad. Sci. U.S.A.*, 2005, **102**, 10451–10453.
112. R. Kappera, D. Voiry, S. E. Yalcin, B. Branch, G. Gupta, A. D. Mohite, and M. Chhowalla, *Nat. Mater.*, 2014, **13**, 1128–1134.
113. A. Kuc, N. Zibouche, and T. Heine, *Phys. Rev. B*, 2011, **83**, 245213.
114. F. Alharbi, J. D. Bass, A. Salhi, A. Alyamani, H.-C. Kim, and R. D. Miller, *Renewable Energy*, 2011, **36**, 2753–2758.
115. A. Gupta, T. Sakthivel, and S. Seal, *Prog. Mat. Sci.*, 2015.
116. S. Jeong, D. Yoo, J.-T. Jang, M. Kim, and J. Cheon, *J. Am.*

Chem. Soc., 2012, **134**, 18233–18236.

117. B. Radisavljevic, A. Radenovic, J. Brivio, V. Giacometti, and A. Kis, *Nat. Nanotechnol.*, 2011, **6**, 147–150.
118. M. Shanmugam, C. A. Durcan, and B. Yu, *Nanoscale*, 2012, **4**, 7399–7405.
119. T. C. Yeh, Q. Zhu, D. B. Buchholz, Martinson, AB, R. Chang, and T. O. Mason, *Appl. Surf. Sci.*, 2015, **330**, 405–410.
120. C.-W. Hsu, L. Wang, and W.-F. Su, *J. Colloid Interface Sci.*, 2009, **329**, 182–187.
121. R. J. Powell, *J. Appl. Phys.*, 1970, **41**, 2424.
122. J. Joo, H. B. Na, T. Yu, J. H. Yu, Y. W. Kim, F. Wu, J. Z. Zhang, and T. Hyeon, *J. Am. Chem. Soc.*, 2003, **125**, 11100–11105.
123. G. Eda, H. Yamaguchi, D. Voiry, T. Fujita, M. Chen, and M. Chhowalla, *Nano Lett.*, 2011, **11**, 5111–5116.
124. Y. Shi, J. K. Huang, L. Jin, Y.-T. Hsu, S. F. Yu, L.-J. Li, and H. Y. Yang, *Sci. Rep.*, 2013, **3**, 1839.
125. A. C. Neto, *Phys. Rev. Lett.*, 2001, **86**, 4382–4385.
126. M. A. Ibrahem, T. Lan, J. K. Huang, Y. Y. Chen, and K. H. Wei, *R. Soc. Chem. Adv.*, 2013, **3**, 13193–13202.
127. H. Kirihata, *Rev. Sci. Instrum.*, 1981, **52**, 68–70.

Appendix I

Supporting Tables and Figures of Chapter 5

Fig. AI.1 shows the UV-vis absorbance spectra for various P3HT:PCBM films deposited on MOE ZnO with cluster area fraction of 0.01 (black), 0.07 (red), 0.34 (green), and 0.46 (blue). The high cluster area fraction films show significant scattering of incident light as indicated by higher absorbance for wavelengths > 650 nm, which is consistent with the large size of PCBM clusters relative to the wavelength.

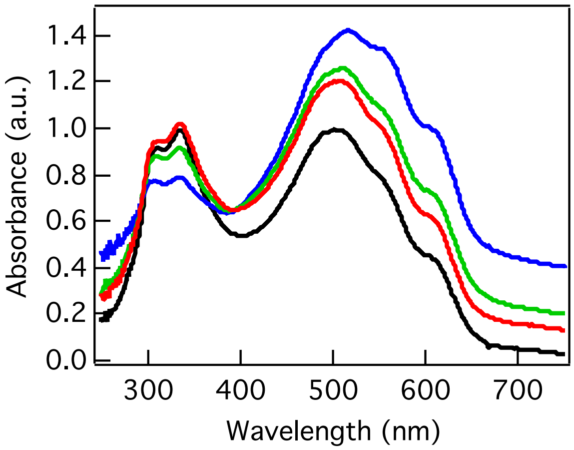

Fig. AI.1. UV-vis absorbance spectra for various P3HT:PCBM films deposited over MOE ZnO with cluster area fraction of 0.01 (black), 0.07 (red), 0.34 (green), and 0.46 (blue).

The dependence of the series resistance (R_{se}) and shunt resistance (R_{sh}) on cluster area fraction is depicted in **Fig. AI.2**. R_{se} increases gradually with respect to cluster area fraction, whereas there is a very little correlation between R_{sh} and cluster area fraction.

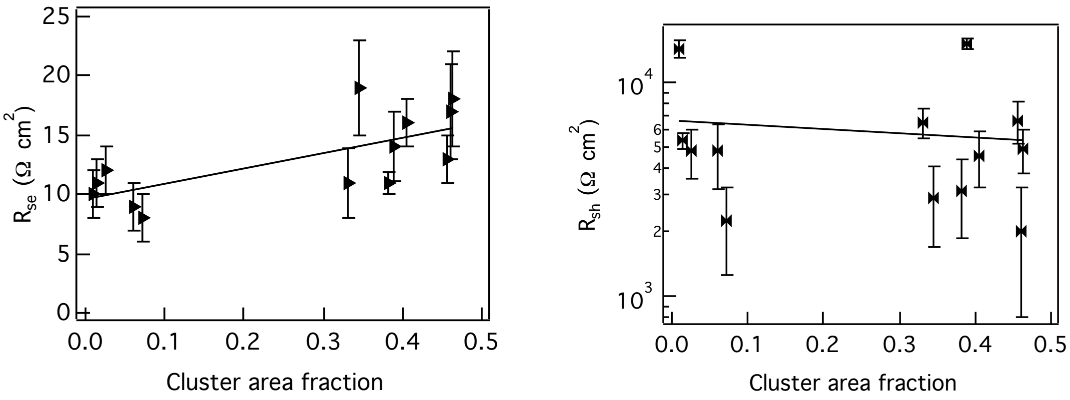

Fig. AI.2. Influence of cluster area fraction on series resistance (right), and shunt resistance (left). Lines correspond to linear best fits.

Fig. AI.3 represents J-V characteristics of rinsed MOE ZnO (**Fig. AI.3**, black) and EtOH ZnO devices (**Fig. AI.3**, blue). Similar performance was observed. Nevertheless, as mentioned in the main text, the absence of a stabilizer makes EtOH ZnO ETL less reliable and reproducible. The OPV parameters for both devices are summarized in **Table AI.1**.

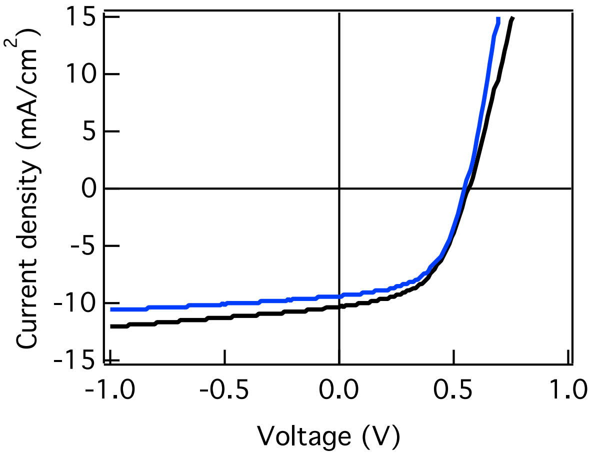

Fig. AI.3. Comparison between MOE ZnO rinsed (black) and EtOH ZnO (blue) on *J-V* characteristics of solar cells under 100 mW/cm^2 AM 1.5G illumination.

Table AI.1. Summary of the device performance parameter of rinsed MOE ZnO and EtOH ZnO obtained from *J-V* characteristics of solar cells measured under 100 mW/cm^2 AM 1.5G illumination.

Sample	**V_{oc} (V)**	**J_{sc} (mA/cm^2)**	**FF ()**	**PCE (%)**	**R_{se} (Ω cm^2)**	**R_{sh} (Ω cm^2)**
rinsed MOE ZnO	0.563 ± 0.005	10.32 ± 0.17	0.518 ± 0.022	3.01 ± 0.10	11 ± 2	5399 ± 476
EtOH ZnO	0.550 ± 0.000	9.36 ± 0.27	0.543 ± 0.023	2.80 ± 0.13	7 ± 2	5937 ± 1976

We found that *J-V* curves of high cluster area fraction devices measured after white-light biased EQE measurements showed a significant degradation, while *J-V* curves of low cluster area fraction devices remained unchanged. **Fig. AI.4** depicts *J-V* characteristics of a

0.01 cluster area fraction device before (black lines) and after (black dashed lines) white-light biased EQE measurements, showing no change. In contrast, the 0.38 cluster area fraction device (**Fig. AI.4**, red) showed clear reduction in J_{sc}, V_{oc}, FF, and PCE after EQE measurement, indicating that these type of devices are susceptible to degradation. The OPV parameters for both devices before and after EQE measurements are summarized in **Table AI.2**. The white-light EQE measurements for each sample took 1.5 hours with continuous light exposure.

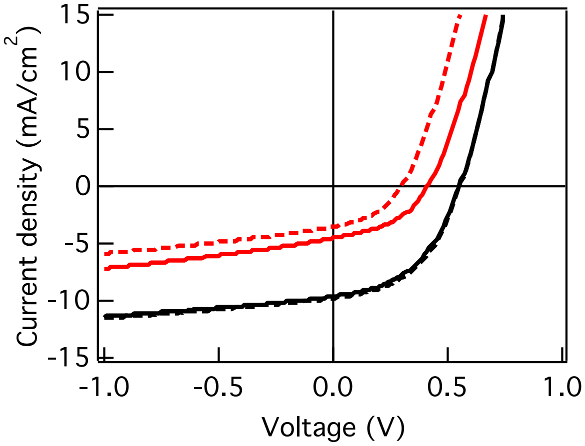

Fig. AI.4. Effect of cluster area fraction on performance reduction of solar cells taken under 100 mW/cm2 AM 1.5G illumination: before (solid line) and after (dashed line) white-light biased EQE measurements for a 0.01 cluster area fraction device (black) and a 0.38 cluster area fraction device (red).

Table AI.2. Summary of the device performance parameter change before and after white-light EQE measurements for devices with two different cluster area fractions.

Sample	V_{oc} (V)	J_{sc} (mA/cm^2)	FF ()	PCE (%)	R_{se} (Ω cm^2)	R_{sh} (Ω cm^2)
Before EQE	0.555 ± 0.005	9.77 ± 0.20	0.475 ± 0.020	2.57 ± 0.16	9 ± 2	3406 ± 1395
After EQE	0.553 ± 0.008	9.63 ± 0.24	0.463 ± 0.026	2.48 ± 0.21	9 ± 2	3326 ± 1471
Before EQE	0.414 ± 0.013	4.52 ± 0.31	0.430 ± 0.007	0.81 ± 0.07	10 ± 2	3800 ± 1443
After EQE	0.296 ± 0.011	3.51 ± 0.23	0.421 ± 0.013	0.44 ± 0.05	10 ± 2	3442 ± 370

Appendix II

Supporting Tables and Figures of Chapter 7

Properties of Metal Oxide NP Suspensions and Films

Size distribution curves of metal oxide NP suspensions in n-butanol from dynamic light scattering are shown in **Fig. AII.1**. As noted in the main text, the dispersed NPs are ~ 1 nm in size, with reasonably narrow size distributions.

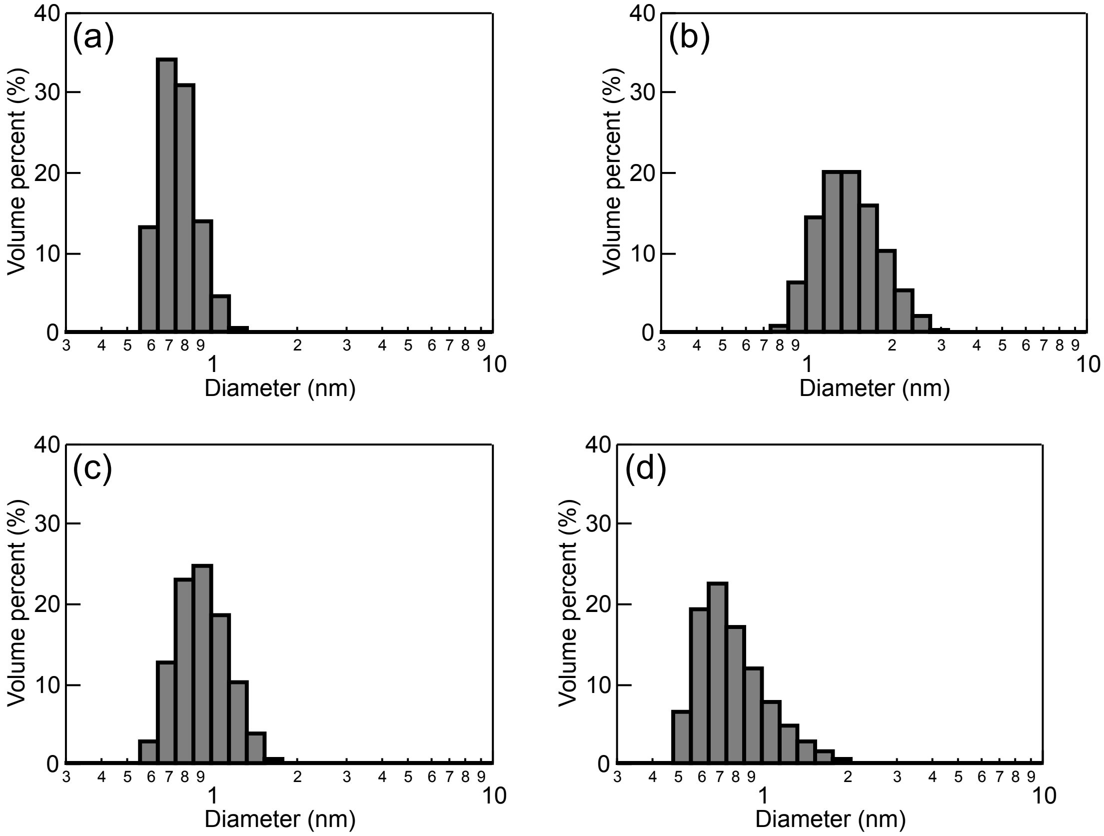

Fig. AII.1. Size distribution curves of (a) MoO_3 NP, (b) WO_3 NP, (c) NiO_x NP, and (d) CoO_x NP suspensions in n-butanol from dynamic light scattering.

For thickness measurements, 0.025M metal oxide NP suspensions were spin coated four times at 8000 rpm on cleaned ITO on glass. Spectroscopic ellipsometry data was collected on a J. A. Woollam M-2000DI, and was fitted between 450-700 nm. The film model used for fitting consists of 1 mm glass ("7059_Cauchy"), 134 nm ITO

(“ITO_parameterized”, fitted previously for bare ITO substrate), and a Cauchy film (k amplitude = 0) for the metal oxide NP film, with zero surface roughness. Good fits were achieved (mean square error < 5), and the fitted metal oxide NP film thickness values are 3.8 ± 0.1 nm for MoO_3, 2.5 ± 0.1 nm for WO_3, 7.6 ± 0.1 nm for NiO_x, and 6.4 ± 0.1 nm for CoO_x. We note that the thickness values are not definitive. For example, if the ITO thickness in the model was decreased to 130 nm, which can easily happen due to batch-to-batch variation from the supplier, the fitted MoO_3 thickness became 7.3 ± 0.1 nm. Nevertheless, the spectroscopic ellipsometry data is in agreement with the WF data showing thin metal oxide NP films are deposited on top of ITO substrates by spin coating.

UPS spectra of MoO_3 NP and WO_3 NP films with He I excitation (21.2 eV) provides information on their work function value and valence band position (**Fig. AII.2**). Φ measured from the photoemission cutoff is 5.5 eV for MoO_3 (**Fig. AII.2a**, left) and 4.9 eV for WO_3 (**Fig. AII.2b**, left). Φ values are similar to the values measured by Kelvin probe for MoO_3 (5.20 eV) and WO_3 (5.31 eV), but with notable discrepancy. The discrepancy may be caused by different degrees of desorption of ambient contaminants when placed in vacuum for UPS, or by photoinduced shifts of the Fermi level in the films under He I excitation. Also, UPS samples a smaller area (~ 150 μm^2) compared to Kelvin probe measurement (~ 3 mm^2), and thus is more susceptible to variations within the NP film. The valence band spectra shows onsets at 3.1 eV for MoO_3 (**Fig. AII.2a**, right) and 3.3 eV for WO_3 (**Fig. AII.2b**, right) that correspond to the difference between Φ and *IE*. Thus, IE is 8.5 eV for MoO_3 and 8.2 eV for WO_3. By subtracting bandgap from IE, EA is found to be 5.55 eV for MoO_3 and 4.75 eV for WO_3. A comparison of Φ and *EA* shows that MoO_3 and WO_3 are *n*-type materials.

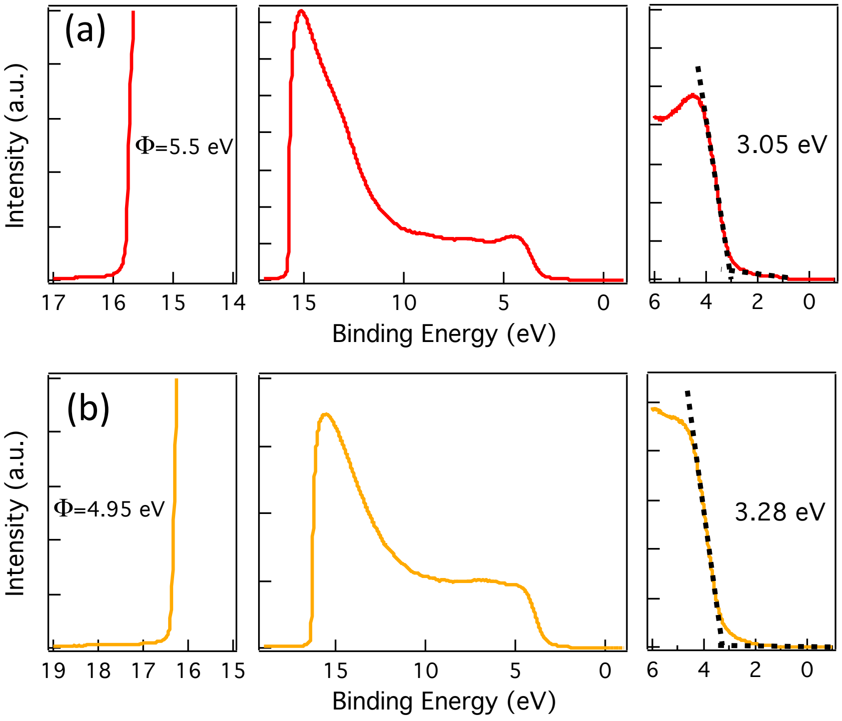

Fig. AII.2. UPS spectra of (a) MoO_3 NP and (b) WO_3 NP films with He I excitation. The photoemission cutoff (left) and valence band spectra onset (right) are shown in expanded scale.

UV-vis absorbance spectra were collected for 0.1M metal oxide NP suspensions. When α^2 was plotted vs. photon energy, where α is the absorption coefficient, for MoO_3 and WO_3 (**Fig. AII.3a**), a linear relationship is observed, and their onset values correspond to direct bandgaps of 2.95 eV and 3.45 eV, respectively. In contrast, NiO_x and CoO_x exhibit multiple absorption features (**Fig. AII.3b**) due to intraband *d*-*d* transitions in addition to the bandgap transition. Thus, literature bandgap values for NiO_x (3.7 eV) and CoO (2.4 eV) were used.

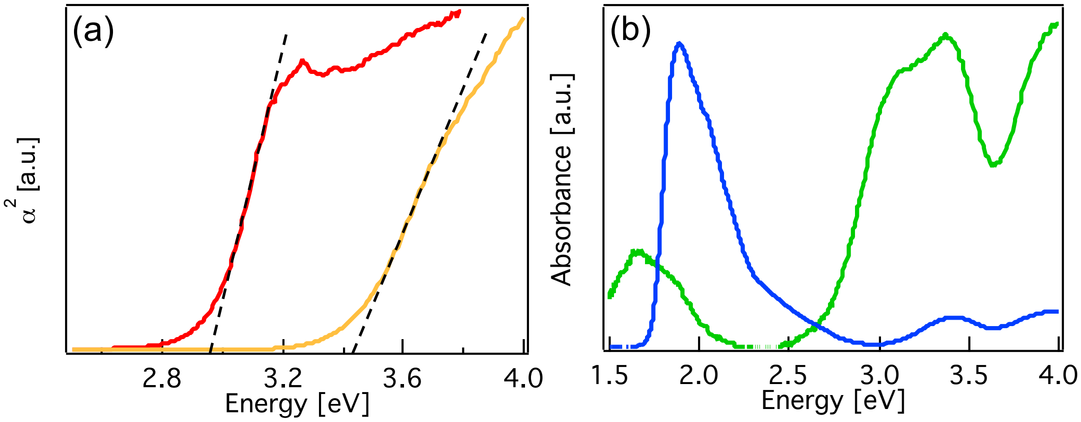

Fig. AII.3. Optical properties of metal oxide NP suspensions in n-butanol. (a) α^2 vs. energy for MoO_3 (red) and WO_3 (orange) NP suspensions. Dash lines indicate the extrapolated bandgap values. (b) Absorbance vs. energy for NiO_x (green) and CoO_x (blue) NP suspensions.

PESA spectra of NiO_x NP and CoO_x NP films show a threshold at photon energy of 5.55 eV and 5.70 eV, respectively (**Fig. AII.4**), which corresponds to their IE. The linear relationship between yield$^{0.33}$ and photon energy indicates that both films are semiconducting[127]. As noted in the main text, the similarity between Φ (5.1 – 5.2 eV) and IE suggests that NiO_x NP and CoO_x NP are *p*-type materials.

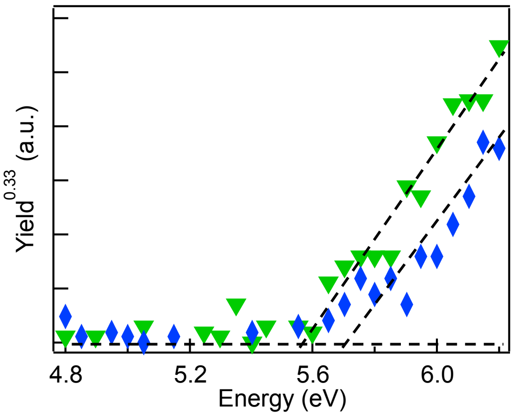

Fig. AII.4. PESA data of NiO$_x$ NP (green inverted triangles) and CoO$_x$ NP (blue diamonds) films, showing onsets corresponding to IE values of 5.55 and 5.7eV, respectively.

The O 1s XPS spectra for NiO$_x$ and CoO$_x$ NP films show contribution from multiple oxidation states (**Fig. AII.5**). As noted in the main text, the NiO$_x$ spectra shows peaks at 529.2 eV, 530.5 eV, and 532.2 eV, corresponding to NiO, Ni(OH)$_2$, and NiOOH, respectively (**Fig. AII.5a**). The CoO$_x$ spectra shows peaks at 529.6 eV, 531.0 eV, and 532.7 eV, corresponding CoO, Co(OH)$_2$, and adsorbed H$_2$O, respectively (**Fig. AII.5b**).

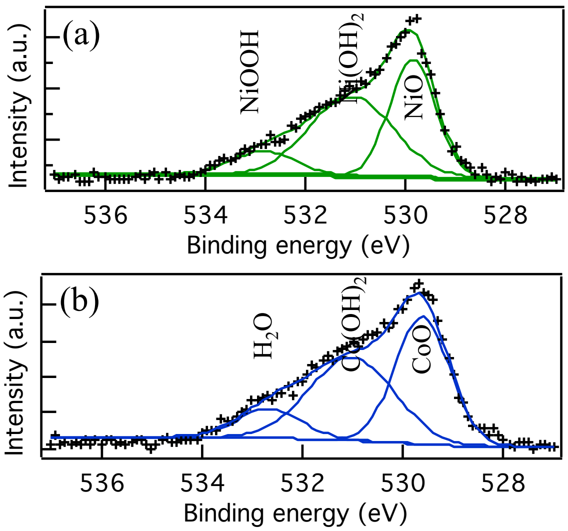

Fig. AII.5. O 1s spectra of metal oxide NP films: (a) NiO_x. (b) CoO_x. Crosses represent experimental data and lines represent fit to the data.

Roughness of metal oxide NP films with optimal thickness values for HTL performance (0.025M for MoO_3 NP, 0.00625M for WO_3, NiO_x, and CoO_x NP) was characterized using atomic force microscopy (Asylum MFP-3D). The root mean square roughness values over a 1 µm x 1 µm area are 1.5 nm, 0.8 nm, 1.1 nm, and 0.9 nm for MoO_3, WO_3, NiO_x, and CoO_x NP films, slightly higher than the ITO substrate at 0.8 nm. This suggests that there are no large aggregates of metal oxide NPs on ITO.

OPV Performance

We examined the performance of metal oxide NP films as HTLs using conventional P3HT:$PC_{61}BM$ OPVs (**Fig. AII.6a**, inset). For metal oxide NP HTLs, metal oxide NP suspensions (0.025M for MoO_3, 0.00625M for others) were spin coated four times at 8000 rpm. Devices with MoO_3 NP HTL (**Fig. AII.6a**, red squares) exhibit performance identical to reference devices with PEDOT:PSS HTL (**Fig. AII.6a**, black circles) under AM1.5 100mW/cm^2 illumination, with a power conversion efficiency PCE of 3.4% (**Table AII.1**). The same PCE was achieved using WO_3 NP (**Fig. AII.6a**, orange triangles) and NiO_x NP (**Fig. AII.6a**, green inverted triangles) HTLs with a thinner thickness by diluting the NP suspensions to ¼ of the concentration before spin coating. Devices with thin CoO_x NP HTL (**Fig. AII.6a**, blue diamonds) exhibit lower V_{oc}, FF, and PCE compared to the reference devices (**Table AII.1**). A comparison of J-V curves for conventional P3HT:$PC_{61}BM$ devices with different HTL thicknesses shows a qualitative difference between devices with MoO_3 NP (**Fig. AII.6b**) and NiO_x NP (**Fig. AII.6c**). For MoO_3 NP, a 4x increase in the concentration of the NP suspension for spin coating (**Fig. AII.6b**, blue) has little effect on the J-V curve, and the device performance is unchanged. In contrast, for NiO$_x$ NP, a 4x increase in concentration generated a S-shaped J-V curve (**Fig. AII.6c**, blue), indicating unbalanced collection of electrons and holes.

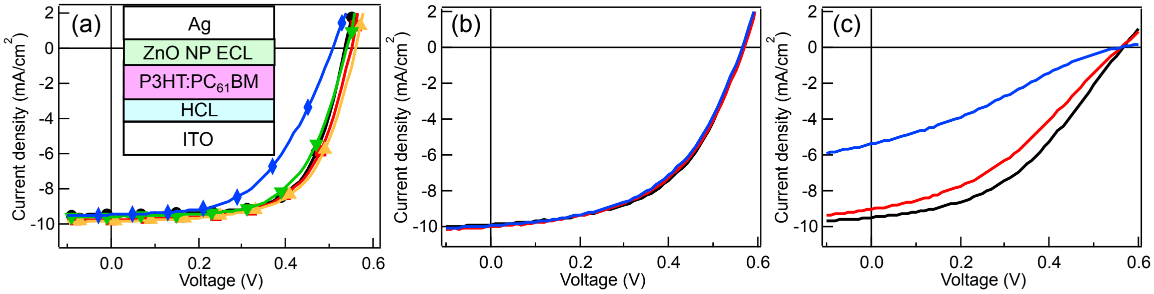

Fig. AII.6. J-V response under AM 1.5 100 mW/cm^2 through a 2.5mm diameter aperture for conventional P3HT:PC$_{61}$BM OPVs with different HTLs. (a) Devices with PEDOT:PSS (black circles), MoO$_3$ NP (red squares), WO$_3$ NP (orange triangles), NiO$_x$ NP (green inverted triangles), and CoO$_x$ NP (blue diamonds). (b) Devices with MoO$_3$ NP spin coated from 0.025M (black), 0.05M (red), and 0.1M (blue) suspensions, showing minimal effect of HTL thickness on performance. (c) Devices with NiO$_x$ NP devices spin coated from 0.0125M (black), 0.025M (red), and 0.05M (blue) suspensions, showing development of a S-shaped curve with increasing HTL thickness.

Table AII.1. Performance of conventional P3HT:PC$_{61}$BM OPVs with different HTLs under AM1.5 100 mW/cm^2 illumination through a 2.5 mm diameter aperture.

HCL	V_{oc} (V)	J_{sc} (mA/cm^2)	FF	PCE (%)
PEDOT:PSS	0.537 ± 0.005	9.48. ± 0.13	0.655 ± 0.012	3.33 ± 0.05
MoO_3 NP	0.550 ± 0.000	9.78 ± 0.13	0.626 ± 0.008	3.37 ± 0.07
WO_3 NP	0.560 ± 0.000	9.87 ± 0.15	0.624 ± 0.018	3.45 ± 0.08
NiO_x NP	0.540 ± 0.000	9.61 ± 0.15	0.617 ± 0.010	3.20 ± 0.04
CoO_x NP	0.506 ± 0.005	9.51 ± 0.16	0.534 ± 0.005	2.58 ± 0.03